Bulletin of the Geological Society of Finland, Vol. 96, 2024, pp 5–34 https://doi.org/10.17741/bgsf/96.1.001

The composition of apatite in the Archean Siilinjärvi glimmerite-carbonatite complex in eastern Finland

Seppo Karvinen[1]*, Aku Heinonen[2], Christoph Beier[1] and Niels Jöns[3]

[1] *Department of Geosciences and Geography, Research programme of Geology and Geophysics (GeoHel), University of Helsinki, PO Box 64, 00014 Helsinki, Finland*

[2] *Geological Survey of Finland, PO Box 96, 02151 Espoo, Finland*

[3] *Ruhr-Universität Bochum, Universitätsstrasse 150, D-44801 Bochum, Germany*

VERTAISARVIOITU
KOLLEGIALT GRANSKAD
PEER-REVIEWED
www.tsv.fi/tunnus

Abstract

We present a geochemical dataset and cathodoluminescence images of apatite from the Neoarchean (2610 Ma) glimmerite-carbonatite rocks from the Siilinjärvi complex, Eastern Finland. The subhedral, tapered prismatic grains are compositionally fluorapatite, with limited substitution of Ca by Sr, Na and low REE and Si contents. The Sr/Y ratios are among the highest in a global apatite comparison, comparable to those from other calcite carbonatites, dolomite carbonatites, and phoscorites. Some grains show evidence of late- or post-magmatic interaction with a carbonatite magma or a hydrothermal fluid, resulting in REE-rich overgrowth rims or recrystallized grains with abundant fluid inclusions. We interpret the high Sr/Y ratios combined with low REE contents and depleted heavy REE+Y to represent crystallization from a mantle-derived carbonatite parental magma. We show that the Siilinjärvi apatite is chemically heterogeneous but with a limited range in compositions. There are noticeable compositional differences on all spatial scales from micrometer to tens of meters, i.e., within a single crystal, between crystals in a sample, between samples and the two individual sampling locations. We conclude that the intra-crystal geochemical variability in apatite is a suitable tracer of the magmatic and post-magmatic evolution of carbonatite complexes.

Keywords: Apatite; carbonatite; mineral chemistry; geochemistry; rare earth elements; trace elements; cathodoluminescence; LA-ICP-MS

*Corresponding author (email: seppo.karvinen@helsinki.fi)

Editorial handling: Shenghong Yang (email: shenghong.yang@oulu.fi)

1. Introduction

Carbonatites are silica-poor and carbonate-rich igneous rocks crystallized from magmas typically derived from the Earth's mantle (e.g., Bell et al. 1998; Mitchell 2005; Yaxley et al. 2022 and references therein). Carbonatites are found in all modern igneous environments, but are typically confined to intracontinental rift settings within cratons and, rarely, erupt at ocean islands (e.g., Schmidt & Weidendorfer 2018). Temporally, they occur from the Mesoarchean to the present, with the majority of dated carbonatites being younger than 650 Ma (Woolley & Kjarsgaard 2008; Humphreys-Williams & Zahirovic 2021). The petrogenesis of carbonatite magmas has been a matter of debate, but currently there are three main models proposed for the formation of mantle-derived carbonatites (see Yaxley et al. 2022 and references therein): 1) very low-degree partial melting of carbonate-bearing or CO_2-rich peridotite or eclogite, 2) formation of an immiscible carbonatite magma through fractional crystallization of a CO_2-bearing, silica-undersaturated magma, or 3) a carbonatitic residual magma evolved from carbonated, alkali-rich, silica-undersaturated magmas.

Carbonatites are of economic interest as they are often enriched in incompatible elements, such as P, rare earth elements (REEs), and Nb (e.g., Chakhmouradian 2006; Anenburg et al. 2020b; Wang et al. 2020; Anenburg et al. 2021). The peculiar enrichment in REEs suggests that the magmas that gave rise to the carbonatites were derived from a metasomatized mantle source with the input of marine sediments (e.g., Hou et al. 2015; Anenburg et al. 2020a). The REE distribution in carbonatites is strongly fractionated, with high ratios of the light REE (LREE) relative to the heavy REE (HREE) (e.g., Hornig-Kjarsgaard 1998).

Apatite is a useful mineral for tracing various geological processes (e.g., Le Bas &Handley 1979; Boudreau and McCallum 1989; Piccoli & Candela 1994; Belousova et al. 2002; Zirner et al. 2015; Mao et al. 2016; Andersson et al. 2019; Bruand et al. 2020, O'Sullivan et al. 2020) and is a mineral commonly present in carbonatites (e.g., Chakhmouradian et al. 2017). Apatites can record a protracted history of crystallization from the carbonatite magma, where its variability in chemical composition reflects the evolution of the magma, which is mainly controlled by the fractionation of calcite ± apatite (Guzmics et al. 2011; Weidendorfer et al. 2017). Recently, there has been a growing number of carbonatite studies utilizing the apatite chemistry to reconstruct the magmatic evolution and to characterize the composition of metasomatic fluids that play a role in the formation of carbonatite-hosted REE deposits (e.g., Broom-Fendley et al. 2017; Chakhmouradian et al. 2017; Slezak et al. 2018; Anenburg et al. 2020a; Decrée et al. 2020a; Lu et al. 2021; Ma et al. 2021; Wei et al. 2022). Studying the composition of apatite in mineralized and unmineralized carbonatite complexes provides information on what processes control the REE enrichment and when these take place in the evolution of the parental magma.

The Siilinjärvi complex (Fig. 1), located in eastern Finland, is among the oldest carbonatites in the world (~2610 Ma, Woolley and Kjarsgaard 2008; Rukhlov & Bell 2010;) and hosts an economic, mined phosphate deposit (Puustinen 1971; O'Brien et al. 2015). The Siilinjärvi rocks are dominantly composed of glimmerites (phlogopite-rich rocks) with varying amounts of banded, intrusive calcite carbonatite veins. All rock types contain abundant fluorapatite (O'Brien et al. 2015). Although the total REE mass fraction in the Siilinjärvi rocks and within the apatites are generally low ($< 2\,000\ \mu g\ g^{-1}$ Total $REE_{whole\text{-}rock}$, Hornig-Kjarsgaard 1998; $< 4\,000\ \mu g\ g^{-1}$ Total $REE_{apatite}$, Decrée et al. 2020b), the REEs could be of economic interest as a by-product of extracting phosphate (Decrée et al. 2020b). Although the Siilinjärvi deposit has been exploited economically for decades, only recently has there been increasing interest in examining the trace element composition of apatite *in situ* and its variability in different units within the Siilinjärvi complex.

Previous studies have quantified the apatite REE content from apatite concentrates, i.e., bulk

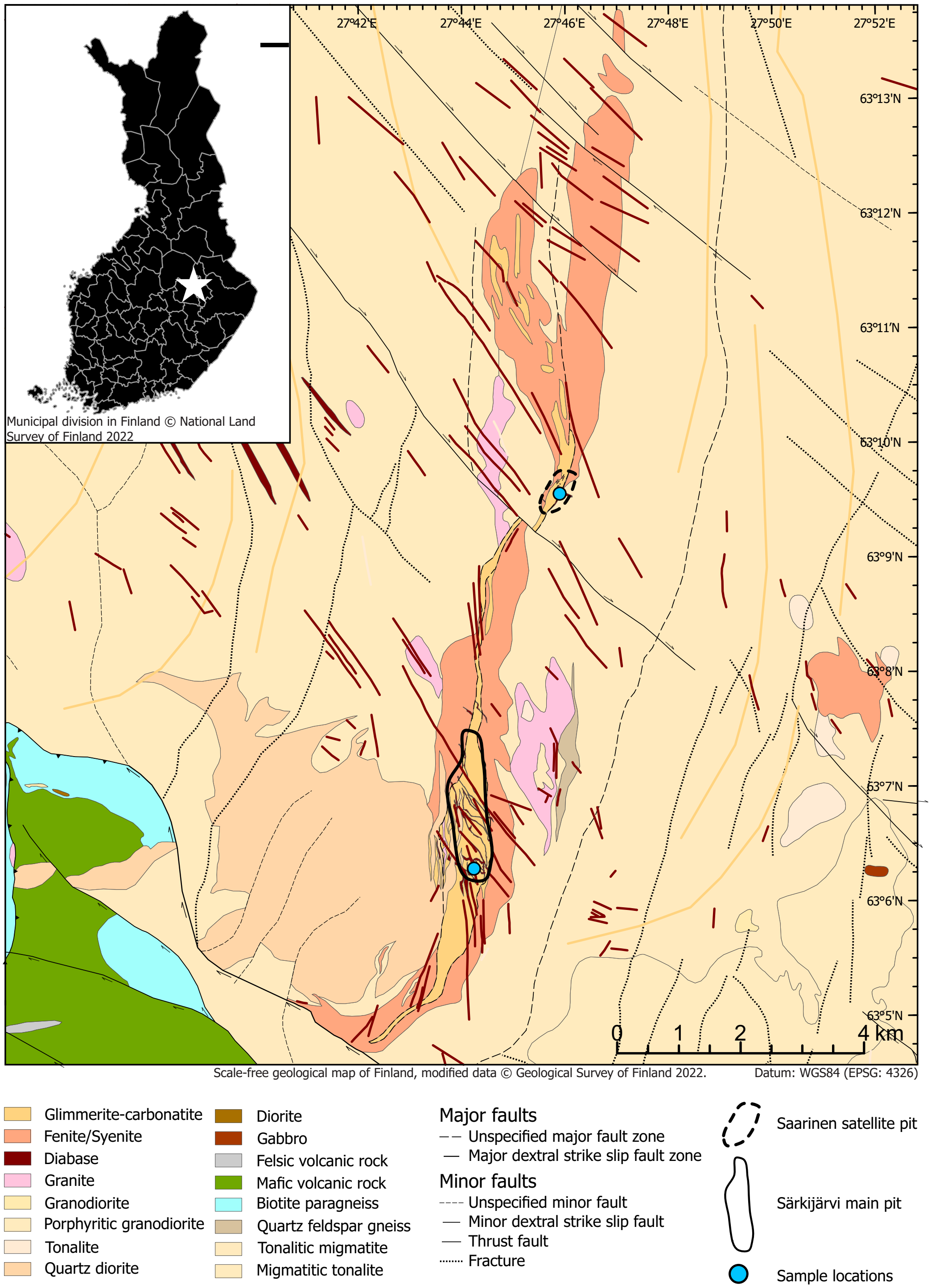

Municipal division in Finland © National Land Survey of Finland 2022

Scale-free geological map of Finland, modified data © Geological Survey of Finland 2022. Datum: WGS84 (EPSG: 4326)

Fig. 1 Geological map of the Siilinjärvi glimmerite-carbonatite complex and the surrounding area. The Särkijärvi pit is highlighted with solid line, Saarinen satellite pit with stippled line. Sampling locations are marked with blue circles. The Inset map shows the location of Siilinjärvi (white star) on the map of Finland. The mine is located some 5 km NE of Siilinjärvi city center.

samples (Puustinen 1971; Hornig-Kjarsgaard 1998), which does not consider the intra-grain variability of the apatite. Decrée et al. (2020b) conducted the first study focused solely on the mineral chemistry of apatite in the Siilinjärvi complex. Their study utilized *in situ* microanalytical methods (EPMA and LA-ICP-MS) and spectroscopic techniques [Raman spectroscopy and, laser-induced breakdown spectroscopy (LIBS), and spectral CL imaging]. Decrée et al. (2020b) describe and quantify the chemical zonation and REE concentrations of apatite in magmatic glimmerite-carbonatites and the surrounding metasomatic fenite.

In this study, we present new *in situ* mineral chemical data of apatite from the Archean Siilinjärvi glimmerite-carbonatite complex, focusing on the compositional variation and differences between the Särkijärvi main pit and the Saarinen satellite pit. We characterize the composition of apatite from 6 samples that span the modal composition of the magmatic glimmerite-carbonatite rock types of the Siilinjärvi complex. We present an extensive major and trace element dataset (182 and 155 analyses, respectively) and discuss our new data in the light of global apatite compositions (3 447 analyses from the literature).

2. Geological background

The Siilinjärvi glimmerite-carbonatite complex is located in the Archean Karelian craton in eastern Finland (Fig. 1), close to the boundary to the Paleoproterozoic province. The Archean province is dominated by tonalite-trondhejmite-granodiorites (TTG), with most of the rocks being Neoarchean in age (2.8–2.5 Ga; Hölttä et al. 2012). The geology of the Siilinjärvi complex has been studied and described first by Puustinen (1971) and, more recently, by O'Brien et al. (2015).

2.1 *Structure, lithology, and mineralogy*

The Siilinjärvi glimmerite-carbonatite complex is a roughly N-trending, 16 km long, up to 1.5 km wide, tabular body which dips 70–90° westwards (Fig. 1; Puustinen 1971; O'Brien et al. 2015). The complex is surrounded by a fenite that comprises metasomatic rocks formed from sodic-potassic alteration of the Archean granite gneiss into which the parental magma intruded (O'Brien et al. 2015). The complex and the country rock are crosscut by at least three generations of mafic dikes with compositions ranging from diabase to lamprophyre (O'Brien et al. 2015; Mattsson et al. 2019). The complex is also cut by a tonalite-diorite intrusion located west and southwest of the Särkijärvi pit (O'Brien et al. 2015; Fig. 1). The complex has an unusual, tabular shape with a sub-vertical plunge (O'Brien et al. 2015) compared to the more common, concentric plug shapes in other carbonatite complexes (e.g., Woolley and Kjarsgaard 2008). In Siilinjärvi, the glimmerite has blocks of fenite within the glimmerite, indicating that exsolution of metasomatic fluids (fenitization) was active already in the early stages of emplacement of the magmatic rocks (O'Brien et al. 2015).

The rock types in the Siilinjärvi complex comprise glimmerites, primarily composed of phlogopite, and varying but subordinate amounts of laminated, currently vertical carbonatite veins, a structure interpreted to be magmatic in origin (O'Brien et al. 2015). The rock types are commonly intermingled and form a series between the glimmerite and carbonatite endmembers. The volume of carbonatite (>50 % modal carbonates) is the most abundant in the center of the complex but, in total, amounts to only about 1.5 % of Särkijärvi intrusion (O'Brien et al. 2015). The fenite rocks are composed primarily of alkali varieties of feldspar, amphibole, and pyroxene.

The carbonatite rocks in Siilinjärvi range in composition from carbonatite with > 50 modal % carbonates to silicocarbonatites with 25–50 modal % carbonates (O'Brien et al. 2015). Calcite is the main carbonate phase, with lesser dolomite occurring as discrete crystals or exsolutions from calcite (Puustinen 1974). Alkali amphibole (richterite, Puustinen 1972), phlogopite, and apatite are the other major phases. Calcite is white to pink in color, and dolomite is gray. Strontianite is also present as small grains (100 µm in width) within calcite (Al-Ani 2013).

The phlogopite in the glimmerite is predominantly tetraferriphlogopite, where Fe^{3+} partially substitutes structural Al^{3+}, but ordinary phlogopite is also present (Puustinen 1973; O'Brien et al. 2015). The mica in the shear zones and in contact with some diabase dikes is altered to biotite or further to chlorite, depending on the intensity of deformation (O'Brien et al. 2015). Richterite, a sodic amphibole, is the main amphibole reported from the complex, but the amphibole minerals display a range of chemical compositions indicating a broader range of amphibole species (O'Brien et al. 2015). Magnetite, sulfides (pyrite, pyrrhotite, chalcopyrite), and zircon are accessory phases. Other rare accessory phases are monazite-(Ce) and pyrochlore minerals (Al-Ani 2013; O'Brien et al. 2015).

The economically exploited phosphate rock from the Siilinjärvi mine contains, on average, 4.2 wt.% P_2O_5 and is modally composed of 65 % phlogopite, 19 % carbonates, 10 % apatite, 5 % richterite, and 1 % accessory phases (O´Brien et al. 2015). The average REE content in the Siilinjärvi rock types is low (< 1 700 µg g^{-1} total REE; Hornig-Kjaarsgard 1998) due to the scarcity of REE-rich phases such as fluorcarbonates, which usually act as REE hosts in mineralized carbonatites (e.g., at Mountain Pass, Castor 2008; Bayan Obo, Fan et al. 2016), and lack of significant REE-enrichment in phases present that do accommodate REE, i.e., apatite.

2.2 Age and petrogenesis

The Siilinjärvi complex is regarded as one of the oldest carbonatites known globally, with the most precise age determinations from zircon U/Pb at around 2 610 Ma (see Rukhlov and Bell 2010 and references therein). The formation of the complex is related to the Neoarchean rifting of the Karelia craton (Rukhlov & Bell 2010; Nironen 2017). The Siilinjärvi complex, including the crosscutting diabase dikes have been altered during the Paleoproterozoic Svecofennian orogeny (~1.92–1.77 Ga, Lahtinen et al. 2014), resulting in greenschist facies metamorphism (Mattsson et al. 2019) and re-equilibrated mineral O, K-Ar, Rb-Sr, and U-Pb isotope systems (Puustinen 1971; Tichomirowa et al. 2006; Rukhlov & Bell 2010).

According to Zozulya et al. (2007), the Siilinjärvi parental magma was related to a moderately enriched mantle source with relatively restricted $\varepsilon_{Nd(T)}$ values of -0.4 to -1.2 and a wide range of $\varepsilon_{Sr(T)}$ values from -2.7 up to +50.5. Zozulya et al. (2007) attribute this range to magmatic fractionation, but it could also be representative of the ratio of phlogopite (Rb accommodating phase) to apatite and calcite (Sr accommodating phases) in the whole rock samples. O'Brien et al. (2015) proposed that the Siilinjärvi complex is the plutonic remnant of a large magma chamber through which highly potassic magmas passed, fractionating minerals forming carbonatite-glimmerite cumulates. The relatively uniform compositions of the tetraferriphlogopite and apatite suggest that the magma chamber was well-mixed enough to fractionate large amounts of minerals with a limited range of compositions (O'Brien et al. 2015).

2.3 Apatite in Siilinjärvi complex rock types

The apatite crystal morphology at Siilinjärvi varies from rounded, subhedral grains to euhedral prismatic grains with lengths varying from submillimeter to dozens of centimeters (Puustinen 1971; O'Brien et al. 2015). The apatite in the Siilinjärvi complex is fluorapatite, with an average of 3.2 wt.% F and 0.75 wt.% SrO (O'Brien et al. 2015). The Sr and Mn concentrations are typical of carbonatites (O'Brien et al. 2015). Geochemical analyses show that the apatite has a relatively low (< 4 000 µg g^{-1}) total REE content and is LREE-enriched, with $(La/Yb)_N$ (chondrite-normalized) ratios of 135–160 (Hornig-Kjarsgaard 1998). These values are corroborated by *in situ* microanalytical analyses where the apatite was found to be slightly less LREE-enriched (La/Yb_N ~100–130) containing 3 000–6 000 µg g^{-1} total REE and 6 600–8 600 µg g^{-1} Sr (Decrée et al. 2020b). The apatite is commonly zoned, visible in CL images where centers of magmatic apatite are characterized by blue to violet colors and overgrowths and rims show in green to yellow colors (Decrée et al. 2020b).

3. Sample material and analytical methods

3.1 Sampling and sample preparation

For this study, Yara Suomi Oy, the mining company operating the Siilinjärvi mine, provided samples from two production pits, the main Särkijärvi pit (63°6.3270'N, 27°44.0508'E) and the Saarinen satellite pit (63°9.5898'N, 27°45.7872'E). Due to high-volume sampling method (blasting), there is no strict structural control for the samples or how they relate to one another, except that they are of 'ore rock' composition, i.e., generally have been defined to contain ≥ 10 % modal apatite. The samples span the whole glimmerite-carbonatite compositional series. Apatite is typically light green, but samples from Saarinen and sample SAR2 from Särkijärvi have darker green apatite.

The rock samples were prepared and studied petrographically at the geophysical, environmental and mineralogical laboratories of the Department of Geosciences and Geography, University of Helsinki (HelLabs). The rock samples were sawed to blocks and sent to a commercial laboratory (Thin Section Lab, Toul, France) to prepare polished thin and thick sections. Thin sections (30 µm) were made from each sample (n=16), and thick sections (100 µm) from six selected samples, three from each pit (Fig 2).

3.2 Petrography

The sections were studied with a petrographical microscope in transmitted and reflected light, after which the thick sections were additionally imaged with a scanning electron microscope (SEM), energy dispersive spectrometry (EDS), and cold cathode cathodoluminescence microscopy (CL). The SEM (JEOL 5800) was operated in high-vacuum mode with 15 kV accelerating voltage. EDS was used to identify small accessory phases. CL imaging was carried out with a CITL CL 8200 Mk5-2, attached to a Leica DM2700 P petrographic microscope with a DFC450 C camera. The CL was operated in automatic mode with a current of 250 µA and an accelerating voltage of 7.5 kV. The samples were re-polished after imaging before being carbon coated for microanalytical analyses.

3.3 Microanalytical methods

3.3.1 EPMA

Apatite was analyzed for major and minor elements with a Cameca SX Five FE wavelength-dispersive electron probe microanalyzer (WDS-EPMA) at the Microanalytical lab of Ruhr-University Bochum, Germany. See Electronic Appendix A for details of the analysis and standards used. The standards, elements, and X-ray lines used were fluorapatite (Ca, P, F; Kα), NaCl (Cl, Kα), albite (Na, Kα), MgO (Mg, Kα), olivine (Si, Kα), $SrSO_4$ (S, Kα; Sr, Lα), spessartine (Mn, Kα), fayalite (Fe, Kα).

Analytical conditions were chosen to minimize electron beam-induced halogen diffusion (e.g., Stormer et al. 1993; Goldoff et al. 2012; Stock et al. 2015). Two analytical methods were used to analyse the main components (Ca, P, F, Cl) and minor components (Na, Mg, Si, S, Mn, Fe, Sr). The primary component method used accelerating voltage and beam current of 10 kV and 4 nA, respectively. In order to ensure that the analyses of halogens were not affected by electron beam-induced diffusion, the time-zero intercept method was applied (e.g., Nielsen and Sigurdsson 1981;

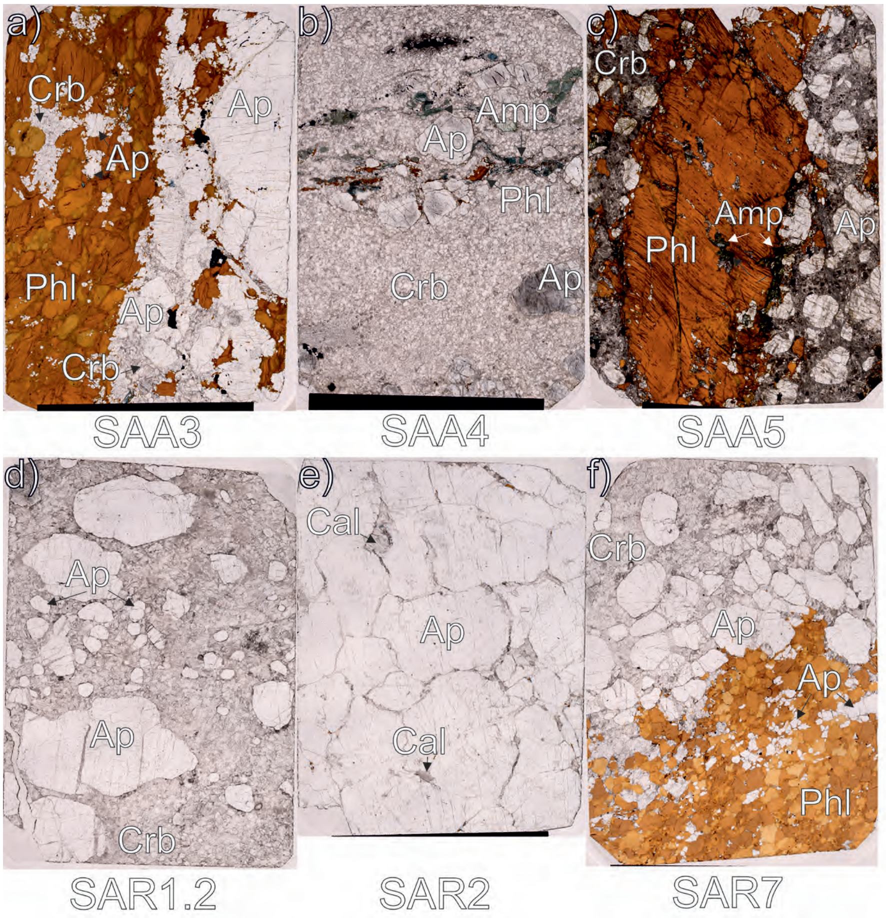

Fig. 2 Photographs of the thick sections studied with micro-analytical techniques. The samples are all primarily composed of carbonates (Crb, mostly calcite; light gray, low relief), apatite (Ap, white, high relief, typically medium to coarse-grained), and phlogopite (Phl, orange-brown in color). Note locally abundant blueish-green amphibole (Amp) in b) and on the rim and within the phlogopite megacryst in c). Apatite is always associated with calcite, even within glimmeritic, phlogopite-rich domains (SAA3 and SAR7). Notice the smaller grain size of apatite within glimmeritic domains. SAA = Saarinen, SAR = Särkijärvi. The dimensions of the thick section are 4.8 cm by 2.8 cm.

McCubbin et al. 2010). For the minor components, accelerating voltage and beam current of 10 kV and 20 nA were used, respectively. A defocused, 10 µm beam diameter was used in both methods. A total of 189 points in 95 grains were analyzed, and 182 points were included in the results. All analyses can be found in Electronic Appendix A. The X-Phi procedure of Merlet (1994) was used to quantify the raw data. Precision and accuracy were checked by repeated analyses on an F-bearing apatite standard (USNM 104021; Jarosewich et al., 1980). Accuracy was better than 1 % for major elements and 3.7 % for F.

3.3.2 LA-ICP-MS

The trace element concentrations of apatite were analyzed by laser ablation inductively coupled mass spectrometry (LA-ICP-MS) at HelLabs. The instrumentation consists of a Coherent GeoLas MV 193 nm laser connected to an Agilent 7900s quadrupole ICP-MS. The system was calibrated and tuned prior to analysis with SRM NIST 610 and analyzing SRM NIST 612 as an unknown.

The surface of the analysis spot was cleaned with a couple of pulses prior to the analysis with a beam diameter larger than the one used in the subsequent analysis (commonly 120 µm). When the ICP-MS signal returned to background levels after the pre-ablation, a gas blank measurement was taken for 40 seconds, followed by an ablation period of 50 seconds and a 30 second washout. The ICP-MS forward power was set to 1500 W, and oxide production was kept at <0.3 %, monitoring ThO/Th ratios, U/Th ratios were set to 100 %.

The apatite was analyzed with an energy density of 6 J/cm^2, a repetition rate of 10 Hz, and a spot diameter of 32–90 µm, depending on the analysis location and the crystal size. The smaller spot sizes were used to analyze the narrow zonation textures visible in CL images and the largest whenever possible. EPMA and LA-ICP-MS analyses were done on the same spots for internal correction. The possible ablation of inclusions or surrounding phases was monitored throughout the analytical sessions and data reduction. The apatite contains ample fine-grained inclusions in some samples, typically carbonate or phlogopite. The inclusion signals were evident on masses ^{24}Mg, ^{27}Al and ^{55}Mn, typically without affecting the primary apatite signal (^{43,44}Ca, ^{31}P, ^{86}Sr, ^{140}Ce). In cases where small inclusions (sharp, short duration peaks) were ablated, the inclusion signal was filtered out, and the constant signal preceding and following the peak was used. Analyses were discarded from results if inclusion signals could not be confidently filtered (n = 34). 155 successful analyses (total = 189) of 94 grains are included in the results. All analyses, including those excluded, are available in Online resource 1.

A total of 33 masses were analyzed: ^{23}Na, ^{24}Mg, ^{27}Al, ^{28}Si, ^{29}Si, ^{31}P, ^{34}S, ^{35}Cl, ^{43}Ca, ^{44}Ca, ^{47}Ti, ^{55}Mn, ^{86}Sr, ^{89}Y, ^{90}Zr, ^{139}La, ^{140}Ce, ^{141}Pr, ^{146}Nd, ^{147}Sm, ^{153}Eu, ^{157}Gd, ^{159}Tb, ^{163}Dy, ^{165}Ho, ^{166}Er, ^{169}Tm, ^{172}Yb, ^{175}Lu, ^{188}Hf, ^{208}Pb, ^{232}Th, ^{238}U.

The trace elements were analyzed in four sessions between May and June 2021. The ^{43}Ca concentrations from the EPMA analyses were used as the internal standard for each specific analysis spot, when possible, and the average CaO concentration of sample, if the analysis spot was not located or unusable due to fractures and inclusions (n = 4). The relative standard deviation (RSD) of CaO wt.% within any sample is <2 %. The apatite analyses were bracketed by analyses of SRM NIST 610, SRM NIST 612, and Durango apatite. Each reference material was analyzed three times before and after the sample analyses and in between during longer sessions every 20–30 sample points. SRM NIST 610 was used as the primary standard for all analyses. Deviation from published standard values (Spandler et al. 2011) was, on average, less than 5 % for all masses, except 6 % for ^{55}Mn (Online Resource 1). The SILLS software (Guillong et al. 2008) was used for data reduction and standardization. GCDKit version 6.3.0 (Janoušek et al. 2006) was used to produce binary trace element and chondrite-normalized REE diagrams.

4. Results

4.1 Petrography

Photographs of the studied thick section samples are shown in Fig. 2. The mineralogy of the samples, apatite textures, and details are summarized in Table 1, and the general petrographic observations are summarized below. All samples are composed primarily of calcite, phlogopite, and apatite in varying abundances and proportions. Sodic amphibole with blue pleochroism is present in some samples typically as euhedral, lozenge-shaped crystals.

Calcite is the most common carbonate, with dolomite occurring as discrete grains within or as exsolutions from calcite. Calcite exhibits polygonal texture with bulging of grain boundaries. Strontianite, observed during the SEM analysis, occurs as very fine grains (<10 µm) within other carbonates. In CL images (Fig. 3), calcite displays a vivid, ruby-red CL signal, whereas dolomite is not CL active. Calcite shows a stronger red CL color near the rim and on the grain boundaries and darker red in the center of grains (Fig. 3a,d). The Saarinen samples have carbonates with fine-grained pigment coating and are inundated with fluid inclusions,

Table 1. Petrographical description of the studied samples.

Sample	Rock type	Mineral paragenesis	Accessory minerals	Apatite size, texture, and inclusions	Apatite CL colors	Description
SAA3	Glimmerite-calcite carbonatite	phl, ap, cal	dol, amp, py, mag, rt	Rounded, anhedral, pigmented, cataclastic crystals, typically 2 mm but up to 8 mm in diameter with ample inclusions, mainly cal. Ap enclosed in phl.	Center: magenta Overgrowth: green Rim: blue, against phl, not always present Sometimes, center-overgrowth colors are inverted	Phl megacryst occupies most of the section. Within the phl, partly in the cleavages, are anhedral ap with minor cal and amph. Amp also rims the phlogopite as an epitaxial growth. The groundmass of the sample is composed of stained cal large, broken, anhedral ap. Deformed phl gives a sense of dextral shear.
SAA4	Calcite carbonatite	cal, ap	dol, phl, amp, mnz, brt, py, ccp	Up to 8 mm euhedral to subhedral, fractured crystals with abundant inclusions of cal mnz and fractures filled with cal and minor py. ~0.04 mm ap in the groundmass, associated with mnz.	Magenta and violet, no clear zonation	Shear zone transects the section, exhibited by zones of fine-grained crb and recrystallized fine-grained ap, associated with mnz and amp and phl lineated with the dominant shear direction.
SAA5	Glimmerite-calcite carbonatite	phl, ap, cal	dol, amp, mag, py, ccp	Subhedral fractured crystals up to 2 mm in size with inclusions of cal and as fracture filling. Ap in the glimmerite domain is always associated with cal, which is in contact with ap. Grain size varies from 0.1 mm up to 2 mm.	Center: magenta Rim: green Some grains show more erratic, discontinuous CL patterns	The sample has a glimmeritic and a carbonatitic domain, dominated by phl and ap+crb, respectively. Ap is always associated with crb, even within phl.
SAR1.2	Apatite-calcite carbonatite	cal, ap	dol, str, brt, mnz	Ap varies from 12 mm to a few mm, fractured, typically subhedral, rounded crystals. The large crystals are more fractured and contain more inclusions than the smaller grains, which can be devoid of fractures and inclusions.	Blue-violet, magenta, and green. Some display chaotic CL patterns, others have violet cores with blue rims against crb groundmass, sometimes with a green overgrowth between the core and rim.	Coarse ap phenocrysts in carbonate (mostly cal) groundmass.
SAR2	Apatitite	ap	cal, mnz, dol, amp, phl, brt	Coarse ap (10–20 mm) with cal as an interstitial phase, fracture filling, and inclusions. Other inclusions are amp, mnz, and brt. Fine-grained ap (<0.2 mm) within interstitial cal between large ap grains are prismatic and stubby in habit and contain no inclusions. Ap displays undulatory extinction.	Coarse ap: dominantly green, differing CL colors give an impression of sub-grains, healed fractures Fine-grained ap: magenta centers, green rims, occasionally green centers, magenta overgrowths, and green rims.	Ap-rich (>90 modal %) carbonatite is formed from partly intergrown ap crystals with cal occurring as inclusions and interstitial filling together with minor phlogopite and amp.
SAR7	Glimmerite-calcite carbonatite	phl, ap, cal	dol, amp, brt, str, pcl, mag	Glimmerite domain has fine-grained anhedral ap associated with carbonate. Carbonatite domain has coarse (1–7 mm) subhedral, occasionally euhedral ap that is cataclastic. There are occasionally round inclusions of cal and phl.	Violet-blue centers, green overgrowths, occasionally blue rims. Some grains have chaotic CL patterns.	The sample has a glimmeritic and a carbonatitic domain, dominated by phlogopite and ap+crb, respectively. ap is always associated with carbonate, even within phlogopite. Brt in groundmass between and in contact with large ap grains.

SAA = Saarinen satellite pit, SAR = Särkijärvi main pit, amp = amphibole, ap = apatite, brt = baryte, cal = calcite, ccp = chalcopyrite, crb = carbonate, dol = dolomite, mnz = monazite, mag =magnetite, pcl = pyrochlore, phl = phlogopite,py = pyrite, rt = rutile, str = strontianite

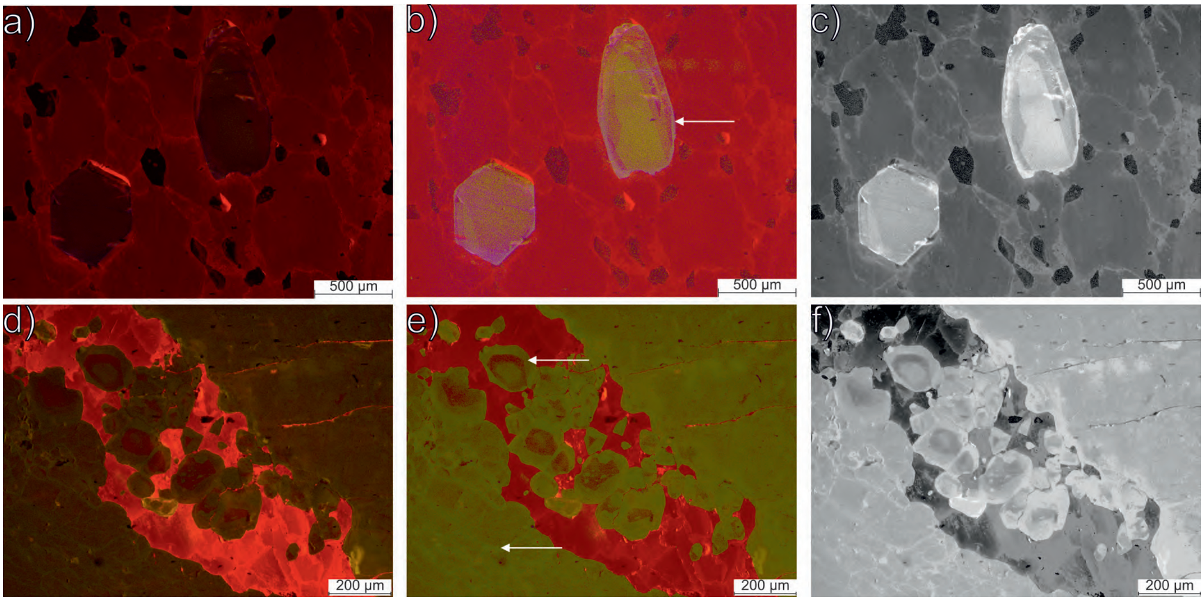

Fig. 3 CL photomicrographs of samples SAR1.2 (first row) and SAR2 (second row). The left column (a, d) is the original CL signal, middle (b, e) and right columns (c, f) are edited image versions where image properties (saturation, contrast, brightness, tone) are altered to highlight differences in CL colors within apatite. Apatite shows blue, violet, and green CL colors in SAR1.2 and green and magenta colors in SAR2. The red groundmass in all pictures is calcite, note the brighter colors on the grain margins of calcite. The CL inactive (dark) phase is dolomite. White arrows in the middle column images (b, e) show CL zonation patterns interpreted in the Discussion section.

giving the carbonates a turbid appearance (Fig. 4c,d).

Phlogopite is the most common silicate mineral in all samples and the most abundant mineral in some samples, usually occurring as glimmeritic domains composed of phlogopite and apatite, associated with minor calcite. The phlogopite displays pleochroism from orange-brown to light colors. Phlogopite exhibits signs of deformation, such as undulatory extinction, bending, and kinking. Phlogopite displays an alteration to chlorite, notable by the change of pleochroic colors from orange to shades of green. Chlorite alteration is more common in samples from Saarinen compared to Särkijärvi.

Apatite is a major phase in all the studied samples, occurring typically as subhedral, rounded, often tapered prismatic crystals from sub-millimeter up to 25 mm in size (Fig. 4). The grain sizes are heterogeneous within samples, most notably in samples with both glimmeritic and carbonatitic domains. For example, in sample SAR7 (Fig. 2f), apatite is, on average, 0.5 mm in length in the glimmeritic domain but shows a wide range in the carbonatitic domain of 0.5–4 mm, with an average of 1.7 mm. Apatite has been affected by brittle deformation, is often fractured or fragmented, and occasionally exhibits undulatory extinction. Recrystallization due to deformation is visible between the contacts of large (> 2000 µm) apatite crystals, where fine-grained apatite (< 100 µm) neocrysts have formed. Calcite occurs as fracture filling and occasionally also as inclusions in apatite. Phlogopite is sometimes found as inclusions in apatite within glimmeritic domains. Fluid inclusions are common in large apatite crystals, especially in samples from Saarinen. The large crystals are typically fractured, whereas fine-grained apatites, which are situated near the grain boundaries of the large crystals, are typically intact and only occasionally contain fluid inclusions. Apatite does not display zonation in BSE images

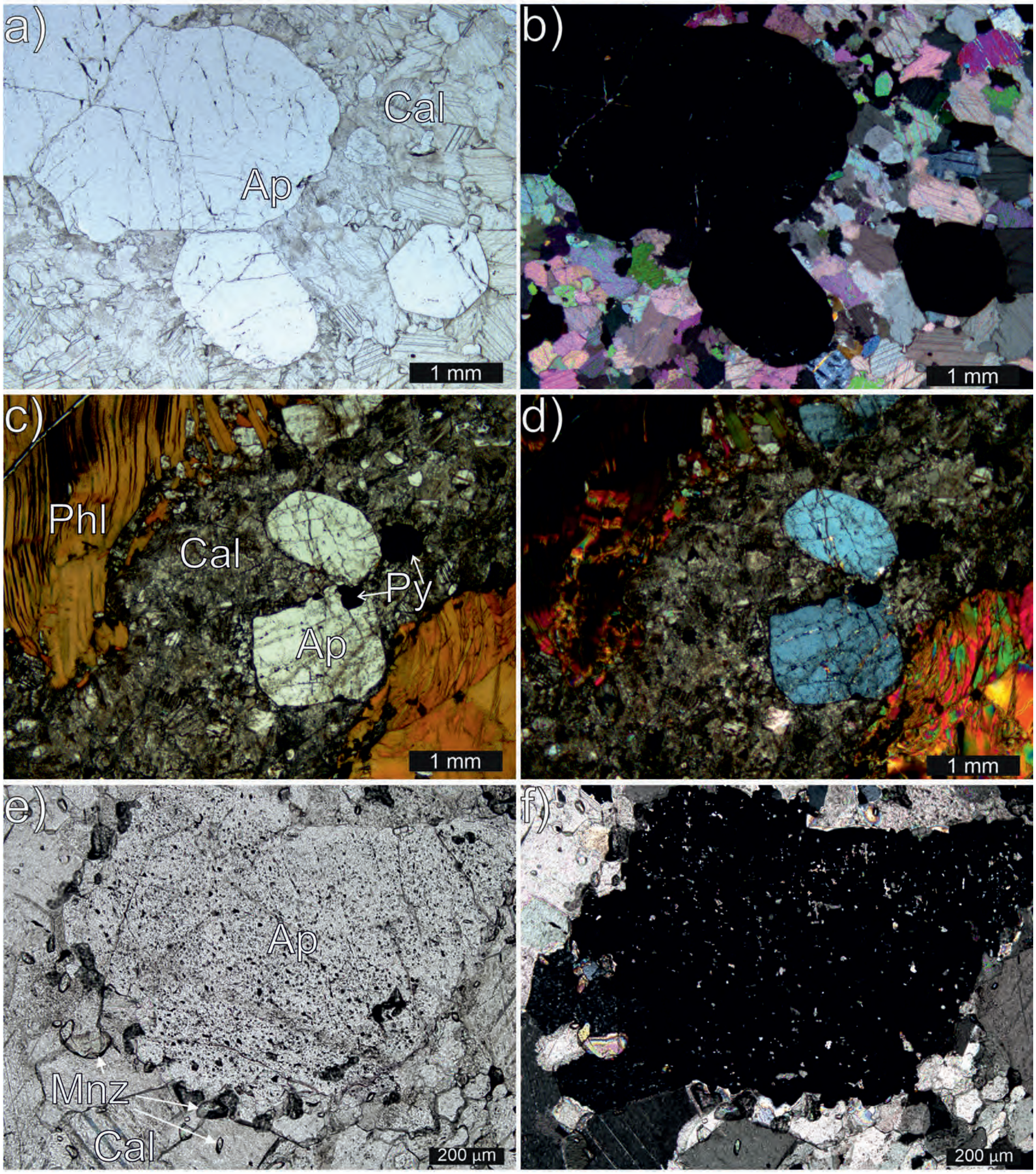

Fig. 4 Different apatite textures in the studied samples. Apatite (white, high relief, fractured crystals) in SAR1.2 (a,b) does not contain many inclusions, whereas apatite in SAA3 (c,d) and SAA4 (e,f) do. In SAA3, a large apatite grain contains inclusions of carbonates as fracture filling. Also, note the pigmented appearance of groundmass carbonates. In SAA4, the anhedral apatite grain has a turbid appearance due to the number of fluid and mineral inclusions (carbonate, monazite). Notice the small monazite grains (high relief and interference colors) on and near the rim and within the apatite. Plane-polarized light on the left column, cross-polarized on the right.

but does exhibit complex zonation in CL images, from simple core-rim zonation to discontinuous, non-systematic patterns with a variety of CL colors. Typical CL colors are green, magenta, blue, and violet. The Saarinen samples more often display green and magenta colors, and the Särkijärvi samples blue and purple, but all samples display a variety of CL colors. The chemical differences and

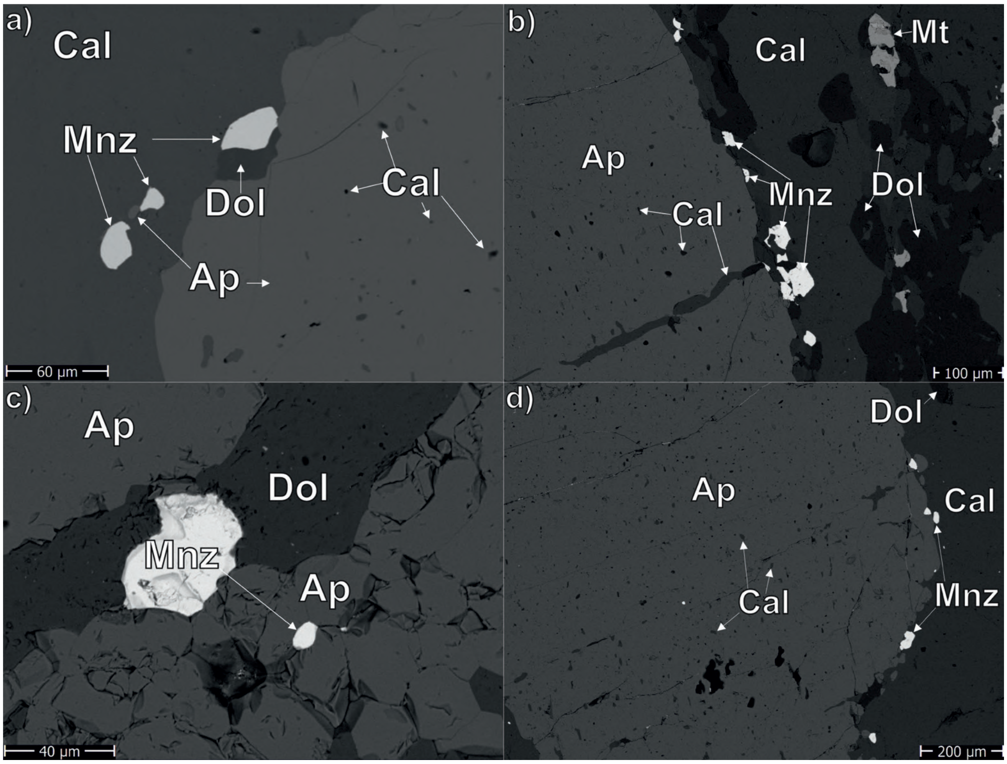

Fig. 5 BSE images of sample SAA4. Coarse-grained apatite (Ap, gray) has ample calcite (Cal, medium gray) inclusions and monazite (Mnz, light gray) grains on the grain margins. Fine-grained apatite does not contain inclusions and is closely packed, with monazite grains on the grain rims (c). Notice that monazite is typically associated also with dolomite (Dol, dark gray). Mag = magnetite.

the petrological implications of these zonation patterns (white arrows in Figs. 3b,e) are discussed later.

Typical accessory phases are monazite, magnetite, baryte, zircon, pyrochlore, rutile, and pyrite, sometimes associated with minor chalcopyrite. Sample SAA4 is transected by a shear zone that is evident from reduced grain size and more abundant occurrence of richterite and phlogopite (Fig. 2b). SAA4 contains abundant monazite grains near the edges of large apatite crystals and in the carbonate groundmass, typically adjacent to fine-grained apatite (Figs. 3e,f; 5). Their formation and petrological significance is discussed in section 5.3. Baryte is observed in most samples, where it is found among carbonates, typically in contact with dolomite or as inclusions in apatite. Magnetite is the most common oxide phase, present as euhedral, fragmented crystals. Rutile is occasionally observed in sheared samples as small (30–200 µm) euhedral crystals associated with phlogopite. Zircon and pyrochlore are uncommon phases observed occasionally in the Särkijärvi samples. Zircon is present as euhedral prismatic crystals up to 500 µm in length. Pyrochlore occurs as anhedral crystals up to 60 µm in length.

4.2 Apatite major element compositions

The chemical and stoichiometric compositions of apatite are presented in Table 2 and summarized below. The entire major and trace element analyses are provided in Electronic Appendix A. The stoichiometric composition is calculated following the method of Ketcham (2015). The hydroxyl component is calculated by subtracting the sum

Table 2. Average major element concentrations of the apatite microprobe analysis. Särkijärvi (main pit), Saarinen (satellite pit). AVG = average, STD = Standard deviation (1σ), RSD = Relative standard deviation, OH* calculated from OH = 2 - (F + Cl) assuming a fully occupied X site.

	Särkijärvi (Main pit)				**Saarinen (Satellite pit)**			
	n = 101				**n = 89**			
	Avg	**Min**	**Max**	**STD**	**Avg**	**Min**	**Max**	**STD**
CaO wt.%	55.05	53.74	56.54	0.59	55.13	53.20	58.23	0.71
Na_2O	0.13	b.d.l.	0.22	0.04	0.13	0.03	0.33	0.07
FeO	0.08	b.d.l.	0.49	0.11	0.08	b.d.l.	0.31	0.09
MnO	0.05	b.d.l.	0.33	0.07	0.06	b.d.l.	0.33	0.09
SrO	0.85	0.68	1.03	0.07	0.67	0.47	0.89	0.08
MgO	0.04	b.d.l.	0.09	0.02	0.07	b.d.l.	0.88	0.13
P_2O_5	42.89	41.37	44.27	0.59	42.72	40.74	43.94	0.53
SiO_2	b.d.l.	b.d.l.	b.d.l.	-	0.01	b.d.l.	0.50	0.06
SO_3	0.02	b.d.l.	0.09	0.02	0.04	b.d.l.	0.30	0.04
F	2.91	2.24	3.55	0.26	2.63	1.76	3.67	0.32
Cl	0.01	b.d.l.	0.05	0.01	0.01	b.d.l.	0.08	0.02
(-O=F, Cl)	-1.23	-1.49	-0.95	0.11	-1.17	-1.55	-0.75	0.14
Ca apfu	9.79	9.60	10.01	0.10	9.82	9.54	10.17	0.11
Na	0.04	0.00	0.07	0.01	0.04	0.01	0.11	0.02
Fe	0.03	0.00	0.10	0.04	0.03	0.00	0.09	0.03
Mn	0.02	0.00	0.07	0.02	0.02	0.00	0.22	0.03
Mg	0.01	0.00	0.02	0.01	0.02	0.00	0.22	0.03
Sr	0.08	0.00	0.10	0.01	0.06	0.05	0.09	0.01
P	6.03	5.94	6.10	0.04	6.01	5.88	6.13	0.05
Si	0.00	0.00	0.00	0.00	0.00	0.00	0.08	0.01
S	0.01	0.00	0.02	0.00	0.01	0.00	0.07	0.01
F	1.53	1.19	1.85	0.13	1.38	0.94	1.90	0.17
Cl	0.00	0.00	0.01	0.00	0.00	0.00	0.02	0.00
OH (2-F+Cl)	0.47	0.15	0.80	0.13	0.62	0.09	1.05	0.17

of F and Cl atoms per formula unit (apfu) from 2, assuming complete occupation of the volatile X-site. The CaO and P_2O_5 concentrations are near the stoichiometric amounts and display little variation, indicating only a limited amount of substitution. Strontium is the most abundant substitute, with mean concentrations of 0.85 ± 0.11 wt.% and 0.67 ± 0.08 wt.% SrO for Särkijärvi and Saarinen, respectively. The Na_2O concentration is 0.13 wt.% on average in both localities. Concentrations of other minor components (MgO, MnO, FeO, and SO_3) are low (< 0.1 wt.%) and, on average, similar in both Särkijärvi and Saarinen.

Apatite from Särkijärvi are, on average, slightly more F-rich (2.91 ± 0.26 wt.%) compared to Saarinen (2.63 ± 0.32 wt.% F), although the differences are subtle and overlap within standard deviation. Chlorine concentrations are below or near the detection limit (< 0.1 wt.% Cl). The apatite from Saarinen have higher calculated hydroxyl concentrations of 0.62 ± 0.13 OH apfu compared to Särkijärvi, which have 0.47 ± 0.13 OH apfu.

4.3 Apatite trace element compositions

The trace element concentrations reveal distinct differences between the apatite from the Särkijärvi and Saarinen pits. The average trace element concentrations are presented in Table 3, binary diagrams (Fig. 6) and a chondrite-normalized REE diagram (Fig. 7).

Apatite from Särkijärvi samples SAR1.2 and SAR7 (Fig. 2d,f) lie along similar trends with limited variation in their trace element compositions (e.g., Fig. 6d,f) whereas sample SAR2 (Fig. 2e) and samples from Saarinen (Fig. 2a–c) show more variation. Concentrations of Sr are, on average, 6 900 ± 570 µg g^{-1} and 5 260 ± 410 µg g^{-1} in Särkijärvi and Saarinen, respectively. Manganese

Table 3. Siilinjärvi apatite average trace element concentrations. Complete analyses are available in Electronic Appendix A. The number of analyses reported for each pit. Rare earth element ratios normalized to CI chondrite values from McDonough and Sun (1995).

	Särkijärvi (Main pit) n = 96				**Saarinen (Satellite pit) n = 59**			
μg g^{-1}	**Avg**	**Min**	**Max**	**STD**	**Avg**	**Min**	**Max**	**STD**
Na	1031	626	1841	223	1095	533	2449	425
Mg	187	35	423	111	243	32	1127	274
Si	234	72	737	143	242	65	730	107
Mn	107	50	250	35	117	66	244	41
Sr	6897	5414	8394	570	5253	4416	6305	413
Y	100.7	73.7	148.0	19.5	95.3	41.6	191.1	33.5
Zr	0.6	0.01	2.00	0.51	0.7	0.01	3.27	0.75
La	645	442	1129	143	533	306	1081	151
Ce	1832	1273	3211	411	1544	966	3105	456
Pr	241	166	415	56	201	133	406	63
Nd	1047	677	1882	255	862	480	1767	284
Sm	153	98	275	37	130	66	261	45
Eu	36.8	23.1	65.5	8.9	32.3	19.4	64.7	11.0
Gd	95.7	61.1	161.7	22.5	82.4	39.4	158.9	27.8
Tb	8.5	5.7	13.8	1.9	7.6	3.5	15.2	2.7
Dy	34.5	24.0	52.3	7.2	31.7	14.4	61.6	11.3
Ho	4.3	3.08	6.62	0.84	4.1	1.78	8.01	1.46
Er	8.3	5.95	11.96	1.55	8.1	3.44	15.60	2.87
Tm	0.7	0.50	1.01	0.11	0.7	0.31	1.41	0.26
Yb	3.2	2.27	4.44	0.51	3.4	1.56	6.41	1.08
Lu	0.3	0.22	0.48	0.05	0.4	0.16	0.69	0.11
Hf	b.d.l.	b.d.l.	0.02	-	b.d.l.	0.01	0.04	0.01
Pb	1.9	0.99	5.05	0.94	7.3	4.27	11.64	1.08
Th	3.5	0.17	11.44	2.16	9.1	0.20	19.51	4.62
U	0.6	0.02	1.39	0.35	1.4	0.01	3.73	1.05
∑REE	4109	2824	7228	936	3440	2238	6951	1043
$(La/Yb)_N$	137	97	189	16	108	77	147	15
$(La/Nd)_N$	1.20	1.03	1.45	0.09	1.21	0.88	1.44	0.12
Sr/Y	70.4	45.0	93.7	10.8	60.8	27.2	132.4	18.6
Th/U	11.8	3.0	80.2	15.9	18.73	4.1	183.7	36.00
Y/Ho	23.7	20.2	29.2	1.4	23.6	21.5	25.3	0.83

concentrations of apatite from the two pits are similar, with an average of 110 μg g^{-1} and 120 μg g^{-1} in Särkijärvi and Saarinen, respectively, but up to 250 μg g^{-1}in Särkijärvi sample SAR2 (Fig. 6e). The Sr and Mn concentrations are similar compared to other carbonatites and overlap with previously published analyses of Siilinjärvi apatite (Hornig-Kjarsgaard 1998; Belousova et al. 2002; O'Brien et al. 2015; Decrée et al. 2020b). Concentrations of Na and Si are, on average, 1 000 and 200 μg g^{-1}, respectively. The contents of Zr, Pb, Th, and U are generally low (≤ 20 μg g^{-1}, Fig. 6e,f), with the lowest concentrations in SAR1.2 and SAR7 and higher values and Th/U ratios in SAR2 and samples from Saarinen.

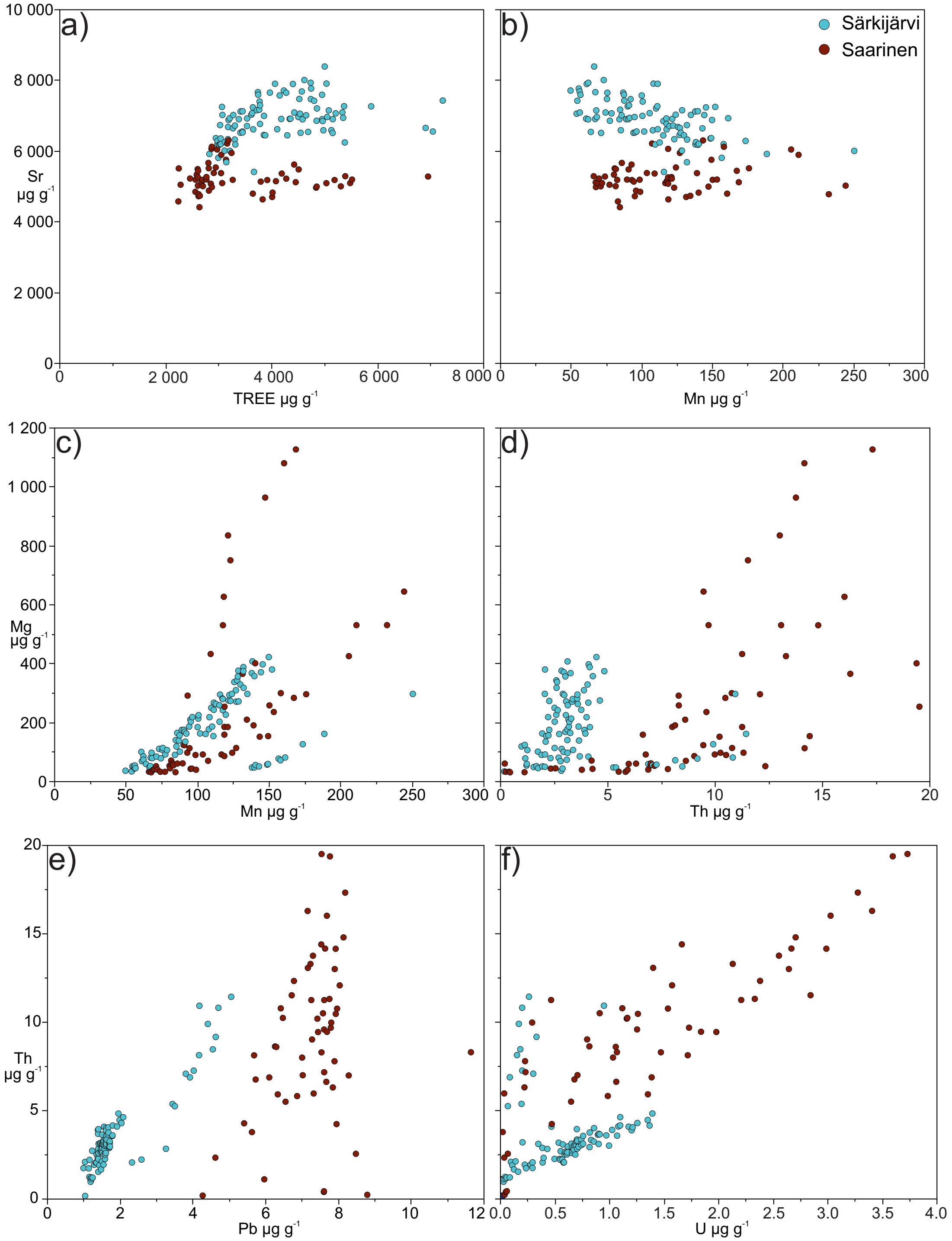

Fig. 6 Apatite trace element scatter plots. SAR1.2 and SAR7 form a series, whereas SAR2 samples have a different composition, more similar to Saarinen analyses. All values are in μg g^{-1}.

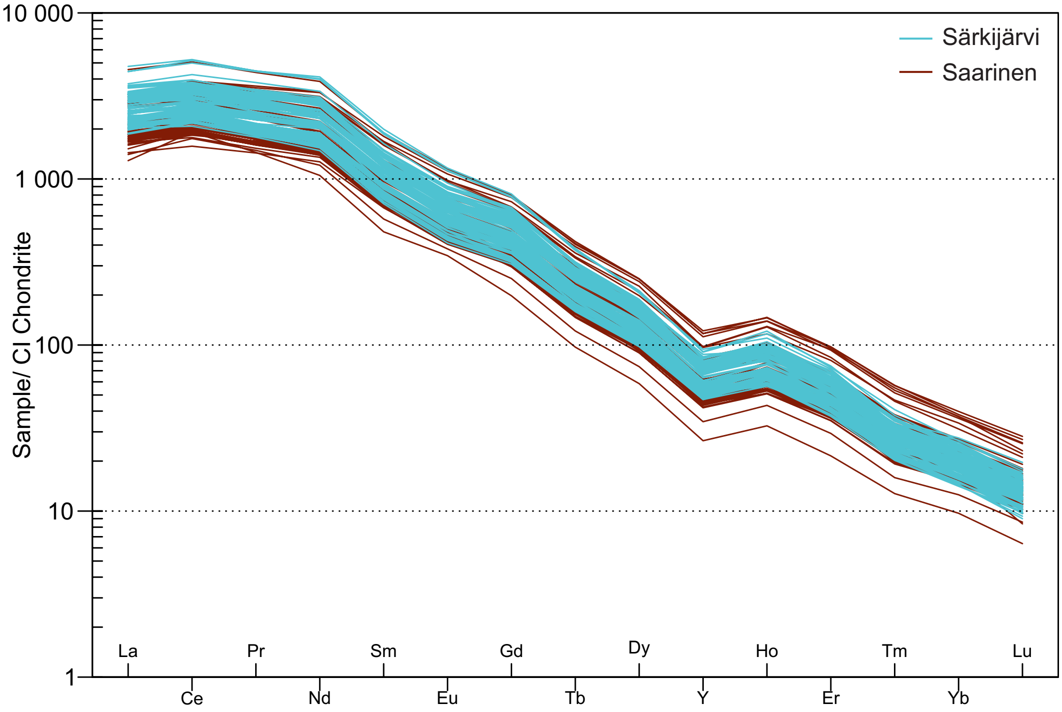

Fig. 7 CI Chondrite normalized rare earth element diagram with yttrium. All analyses display a strong fractionation pattern seen as high La/Yb ratios.The REE patterns from La to Nd are near unity and all samples display a negative Y anomaly. Särkijärvi samples in blue, Saarinen in green. CI Chondrite values from McDonough and Sun (1995).

The apatite are strongly fractionated in REE as shown by their $(La/Yb)_N$ of ~137, and they are characterized by relatively flat patterns from LREE to MREE with $(La/Nd)_N$ ratios of 1.2 (Fig. 7). The average total REE concentrations in Särkijärvi are 4 110 ± 930 µg g^{-1}. In Saarinen, the total REE concentrations are lower (3 430 ± 1 035 µg g^{-1}) but overlap with variation. The $(La/Yb)_N$ ratio in Saarinen is lower than in Särkijärvi (107), whereas the $(La/Nd)_N$ ratios are comparable. The REE concentrations are not correlated with Na or Si (Electronic Appendix C). The highest total REE concentrations (~7 000 µg g^{-1}) were observed in a few CL overgrowths and/or rim zones in sample SAR.1.2 and in recrystallized apatite in sample SAA4. Some of the apatite in SAA4 are also relatively depleted in LREE (lower $(La/Yb)_N$) and enriched in MREE relative to HREE and Y.

Cerium (Ce/Ce*) and Eu (Eu/Eu*) anomalies display little variation between Särkijärvi and Saarinen. The values are slightly above and below unity in both localities, respectively. The Y/Ho ratios are sub-chondritic, and when plotted on a chondrite-normalized REE+Y diagram, all samples display a negative Y anomaly (Fig. 7). The Sr/Y ratios have an average value of 70 and range from 45 to 94 in Särkijärvi and 61 and 27–133 in Saarinen, respectively. The Sr/Y ratios correlate negatively with total REE concentrations.

5. Discussion

The Siilinjärvi apatite has higher Sr/Y ratios than other magmatic carbonatite apatite with higher Sr concentrations, such as the Miaoya and Shanxiodong carbonatites in China (Zhang et al. 2019; Lu et al. 2021), Oka, Canada (Chen and

Simonetti 2013) or in shonkinites in Mountain Pass, USA (Poletti et al. 2016). The high Sr/Y ratio is the result of the strong depletion of Y and HREE and a mild enrichment in Sr. Here, we discuss the geochemical signatures of the Siilinjärvi apatite from a magmatic and fluid-related perspective and compare them with the global apatite dataset. We interpret the Siilinjärvi samples to represent an end-member composition amongst the global magmatic apatite array, the geological and petrological significance of which will be discussed in further detail below.

5.1 Substitution of REE into apatite structure

The incorporation of REE in apatite is typically the result of a coupled substitution with either Si (Eq. 1, britholite substitution), Na (Eq. 2, belovite substitution) or by structural vacancies (Eq. 3, Watson and Green 1981; Roeder et al. 1987; Rønsbo 1989; Hughes et al. 1991; Fleet and Pan 1995). During britholite substitution (Eq. 1), the REEs are facilitated into the structure of apatite by changes in both M and T sites, the latter being primarily occupied by P. The belovite substitution (Eq. 2) takes place in the M sites, which are primarily occupied by Ca in apatite group minerals.

$$\mathrm{REE}(^{3+})+\mathrm{Si}(^{4+})\leftrightarrow\mathrm{P}(^{5+})+\mathrm{Ca}(^{2+})\ \text{(Eq.1)}$$

$$\mathrm{REE}(^{3+})+\mathrm{Na}^{+}\leftrightarrow 2\mathrm{Ca}(^{2+})\ \text{(Eq.2)}$$

$$2\mathrm{REE}(^{3+})+\square\leftrightarrow 3\mathrm{Ca}(^{2+})\ \text{(Eq.3)}$$

The enrichment involving Na substitution requires strongly peralkaline conditions, whereas the substitution with Si occurs in non-peralkaline to slightly peralkaline conditions (Rønsbo 1989). Increasing Si activity and decreasing temperature correlate positively with REE partitioning into apatite in experimental melts of basanitic to granitic compositions (Watson and Green 1981). A high Si activity also has a similar effect in carbonatitic melts (e.g., Klemme and Dalpé 2003; Anenburg et al. 2020b; Sartori et al. 2022), where high-temperature primary fluorapatite is not enriched in REEs. Hence, here we focus on the magmatic signatures and the fluid-induced changes in the mineral chemistry of the Siilinjärvi apatite.

5.2 Magmatic signatures in the Siilinjärvi apatite

In Siilinjärvi, apatite represents an early crystallising phase based on petrographic evidence. Apatite is typically a subhedral phase within a carbonate matrix composed primarily of calcite. Inclusions of other major phases, such as calcite and rarely phlogopite, are found within apatite. In glimmeritic domains, apatite is typically enclosed in phlogopite, together with calcite (Fig. 2a,f). We did not observe compositional differences between apatite compositions in samples from the distinct carbonatite and glimmerite domains e.g., in SAR7 (Fig. 2f). The Sr/Y ratios in Siilinjärvi apatite are high, on average 67 ± 15, with a noticeable range between samples and between pits. Särkijärvi apatite has higher average Sr/Y ratios compared to Saarinen. In samples SAR1.2 and SAR7, the apatite displays a wide range of Sr/Y, exhibiting a negative correlation with increasing REE concentrations, as Y correlates positively with the REE. Contrastingly, the Sr/Y ratios in sample SAR2 have a narrow range (72–85). The highest Sr/Y ratios are found from sample SAA5 in apatite with green CL and low REE concentrations.

Siilinjärvi apatite has generally low total REE concentrations (~3 800 µg g^{-1}), compared to apatite from other carbonatites (e.g., Hornig-Kjarsgaard 1998; Mao et al. 2016; Chakhmouradian et al. 2017; Lu et al. 2021). These results agree with the previous study on the Siilinjärvi apatite (Decrée et al. 2020b). The few outliers with the highest REE concentrations (Fig. 6a, ~7 000 µg g^{-1} TREE) are exclusively analyzed from the rims of zoned apatite (Fig. 3a,b,c) and in the center of fine-grained apatite in the carbonate groundmass. In sample SAR1.2, the REE-enriched rims are narrow zones on the outer part of grains with elevated $(\mathrm{La/Yb})_N$ ratios and a blue CL color (Fig. 3a). A blue CL signal in apatite has been attributed to Ce^{3+}, Eu^{2+}, and Sm^{3+} and Nd^{3+} (e.g., Kempe and Götze 2002, Slezak et al. 2018, Decrée et al. 2020b) but can also be caused by O electron defects in the structural phosphate group (Habermann et al. 1997 in Götze 2012). However, based on our combined observations, we propose that the blue CL colors reflect an enrichment in the REE.

Our results show that the apatite crystals are often chemically zoned and heterogeneous within and between samples and between the two sampling locations, suggesting that the variability within and between different samples is high. The linear trends and limited range in trace element concentrations in samples SAR1.2 and SAR7 are interpreted to represent magmatic differentiation. The differences in apatite compositions between Särkijärvi and Saarinen may be caused by magmatic evolution, Saarinen being derived from a more fractionated magma or divergent post-magmatic processes such as the influence of intruding diabase dykes and their thermal influence (Ranta et al. 2018) or deformation induced recrystallization, since the Saarinen pit is located near the contact with the Archean country rock. The low Si and REE concentrations of the Siilinjärvi apatite can best be explained by crystallizing early from a carbonatite magma with low Si activity, as REEs are incompatible in fluorapatite at magmatic crystallization temperatures (Anenburg et al. 2020b). The blue CL rims are thus likely formed by the crystallization of REE-enriched apatite rims from a later-stage fractionated magma enriched in REE, also suggested by Tichomirowa et al. (2006) and Decrée et al. (2020b), a REE-enriched brine-melt (Anenburg et al. 2021) or with a REE-bearing fluid during late stages of crystallization (Broom-Fendley et al. 2017). This enrichment is not observed in all samples, which suggests that the spatial variability in REE enrichment may be localized or uncommon.

Apatite-fluid interactions can locally affect the modal composition and the abundance of REE in mineral phases (e.g., Broom-Fendley et al. 2016). These processes can be traced with changing apatite compositions (volatile composition, REE patterns and concentrations, and Sr/Y ratios).

5.3 Fluid signatures in the Siilinjärvi apatite

Sample SAR2 is mainly composed of coarse (up to 20 mm) apatite (Fig 2e) that is uniform in plane-polarized light but shows zonation and internal structures in the CL images (Fig. 3d,e,f). Some coarse apatite grains have formed from several previously separate grains that have grown together, as shown by different intergrown center-rim CL zones (Fig. 3d,e,f). Fine-grained apatite that displays complex compositional zoning in the CL images occurs between the coarse apatite composite grains within the interstitial calcite. The center-overgrowth-rim zonation texture shows green-purple-green CL colors. Similar textures have been reported from Chipman lake and Schryburt lake carbonatites from Canada (Chakhmouradian et al. 2017).

The fine-grained apatite in SAA4 may represent recrystallization products by a complex dissolution-reprecipitation mechanism (e.g., Harlov et al. 2005; Putnis 2009; Broom-Fendley et al. 2016). The relatively hydroxyl-rich (up to 53 % or 1.05 apfu OH^- component) nature of the apatite in SAA4 reflects crystallization in a halogen-poor fluid environment, as hydroxylapatite is only stable in fluids with low Cl and F activities (Harlov 2015). Fluorine is challenging to analyze in apatite due to electron beam-induced halogen diffusion and crystallographic effects (e.g., Stormer et al. 1993; McCubbin et al. 2010; Stock 2015), although our EPMA method was explicitly chosen to minimize such effects. An alternative explanation is that the unanalyzed component is structural carbonate or oxygen (oxyapatite component) instead of OH^-. Substitution of carbonate coupled with F can result in super-stoichiometric F concentrations (>3.77 wt.% F; Binder and Troll 1989; Tacker 2008; Yi et al. 2013), which is not observed in our analyses. However, structural carbonate seems common in carbonatite-derived apatite and is not always coupled with high F concentrations (Broom-Fendley et al. 2021). The oxide totals for EPMA analyses were, on average, 100.7 wt.%, indicating no major unanalyzed components. Thus, we interpret the lower F concentrations to represent OH-rich apatite formed in a post-magmatic, F-poor environment.

The relative enrichment of HREE+Y in sample SAA4 and the abundant crystallization of monazite could have been caused by fluid-induced metasomatism, where apatite reacted with the fluid such that the LREEs were preferentially leached, together with P. The original apatite underwent recrystallization, and the LREEs and P in solution precipitated as monazite near or at the apatite. This phenomenon has been reported from experimental petrology and natural systems (Harlov and Förster 2003; Harlov et al. 2005; Antignano and Manning 2008; Ma et al. 2021; Su et al. 2021). Experimental works (Harlov et al. 2002; Harlov and Förster 2003; Harlov et al. 2005) show that monazite can form from an interaction of a hydrous metasomatic fluid with fluorapatite. High CO_2 activity in the metasomatic fluid inhibits monazite growth based on its absence in experiments with a high CO_2/H_2O ratio in the fluid (Harlov and Förster 2003). We interpret the fine-grained apatite in sample SAA4 to have formed by dissolution-reprecipitation reactions in which monazite crystallized as a result of interaction between apatite and hydrous fluids in the shear zone.

Fluid-apatite interactions have also taken place within the metasomatically formed fenite aureole. Decrée et al. (2020b) reported britholite overgrowths on an apatite grain in a pyroxene-rich fenite sample (sample Si6 in Decrée et al. 2020b). Britholite is a REE-silicate mineral group within the apatite supergroup (Pasero et al. 2010). Decrée et al. (2020b) do not present mineral chemical data for the britholite. However, the immediate association of apatite and britholite can be interpreted as a local effect of alkali-rich, fenitizing fluid, which has leached silica from the host rock protolith (granite gneiss) and reacted with apatite precipitating REE and Si as britholite on the apatite grain surface. This process, often referred to as an antiskarn, can concentrate REE, potentially to economic concentrations (e.g., Nolans Bore, Australia; Anenburg et al. 2020a; Miaoya, China; Ma et al. 2021).

5.4 Formation of the Siilinjärvi complex from apatite compositions

The Siilinjärvi complex has an unusual, Y-shaped form on the current erosional level (Fig. 1), likely due to deformation during the Svecofennian orogeny, compared to the more common, concentric shapes of other carbonatite complexes (e.g., Woolley & Kjarsgaard 2008).

Due to the similar mineral assemblage and chemical composition, O´Brien et al. (2015) suggested that the lamprophyre dikes that crosscut the complex could represent the parental magma composition of the Siilinjärvi glimmerite-carbonatites. However, they also note that the concentration of P is too low, and the concentration of Fe is too high, as the Siilinjärvi rocks contain ample apatite but no Fe-rich (i.e., magnetite) cumulates. The glimmerite, the most common rock type in the Siilinjärvi complex (O'Brien et al. 2015), is an Fe-rich rock (8–9 wt.% FeO, O’Brien et al. 2015, Decrée et al. 2020b), and as such, could potentially be the host of this excess Fe. The accumulation of apatite increases the concentration of P_2O_5 in the rocks (O’Brien et al. 2015, Decrée et al. 2020b), and there are near monomineralic apatite rocks in the complex (e.g., Sample SAR2 in this study).

Mattsson et al. (2019) further studied the different dike rock types in the complex and argued that the lamprophyre magma could represent the parental magma of the carbonatite rocks. Mattsson et al. (2019) introduced a model where a parental lamprophyre magma evolved through fractional crystallization to the point of immiscibility, where a moderately alkaline carbonatite magma exsolved from the parental silicate magma. The alkali-rich carbonatite magma then ascended further through the crust. The residual silicate magma intruded the complex as foiditic and ultrapotassic (molar ratio of $K_2O/Na_2O > 3$), and mafic dikes ('Group A dykes' in Mattsson et al. 2019). The lamprophyre dikes in the Siilinjärvi complex are Mg-rich (up to 31 wt.% MgO), peralkaline, and ultrapotassic (Mattsson et al. 2019). The single lamprophyre whole-rock analysis presented by Mattsson et al. (2019) has a strongly fractionated REE profile (La/Yb_N of ~72) and a high (128) Sr/Y ratio. The petrogenetic model of Mattson et al. (2019) does not involve the formation or role of glimmerites in the Siilinjärvi complex even though glimmerites are the most abundant rock type. The glimmerites could represent the metasomatic product of magma-wallrock interactions (Vasyukova and Williams-Jones, 2022), but investigating this is beyond the scope of this paper.

Based on our petrographical observations and mineral chemical analyses, the magmatic composition of Siilinjärvi apatite is best preserved in samples SAR1.2 and SAR7 from the Särkijärvi pit, where apatite is present as rounded, typically subhedral grains that contain little inclusions. This rounded habit of fluorapatite in plutonic carbonatites has been interpreted to be the result of erosion of crystal faces in magmatic abrasion during the ascent of the parental magma (Chakhmouradian et al. 2017; Anenburg et al. 2020a). Despite also showing signs of post-crystallization deformation and limited changes in chemical composition, the apatite analyzed from these samples shows a narrow compositional range that we interpret to represent continued fractionation from the parental magma. We interpret the strongly fractionated REE composition, HREE+Y depletion and high Sr/Y ratio in Siilinjärvi apatite to have been inherited from the parental magma that was likely sourced from carbonated mantle, supporting the petrogenetic interpretation of Mattsson et al. (2019). We will next introduce a global apatite trace element database and discuss the trends of magmatic and post-magmatic processes and how they may affect apatite compositions.

5.5 The Siilinjärvi apatite in a global comparison

Apatite trace element concentrations and element ratios have previously been used to identify their host rocks (Belousova et al. 2002) and to discern apatite from mineralized and unmineralized lithologies (e.g., Mao et al. 2016; Lu et al. 2021). Lu et al. (2021) collected a database ('Appendix A' in Lu et al. 2021) consisting of their own apatite trace element results from carbonatite-hosted REE-deposits in China with previously published apatite results from a variety of host rock types, spanning silicate rock types from felsic to ultramafic, a variety of alkaline rock types, carbonatites, and several different types of mineralizations. Here, we expand this database with our new data and other relevant published data (Electronic Appendix B) and show that apatite trace element chemistry can be used to broadly distinguish the petrogenetic environment and post-magmatic processes. Apatite from ultramafic mantle xenoliths, carbonatites, and alkaline rock types and associated ultramafic rocks are the most enriched in Sr (>2 000 $\mu g\ g^{-1}$) and have the highest chondrite-normalized $(La/Yb)_N$ (typically >100, not shown) and Sr/Y ratios (>10). This trend is evident in Sr/Y ratios versus Sr, Y, or Yb. The enrichment of HREE+Y causes analyses to deviate from the magmatic trends (Fig. 8 and 9). The other endmember of the trend is defined by felsic rocks, which have apatite with variable but lower Sr that are relatively enriched in Y and HREE, resulting in lower Sr/Y. This trend reflects the magmatic evolution and crystallization from highly fractionated melts (e.g., Belousova et al. 2002; Lu et al. 2021). Magmatic carbonatite apatite typically displays a negative Y anomaly relative to Dy and Ho in chondrite-normalized REE diagrams (Bühn et al. 2008; Chakhmouradian et al. 2017; Broom-Fendley et al. 2021). Apatite from altered carbonatites, overprinted by carbo-hydrothermal fluids ('Fluid-driven' category in Lu et al. 2021, 'Carbonatite (Metasomatic)' in Figs. 8, 9) form a separate trend that plots away from apatite from primary, magmatic carbonatites, sometimes with

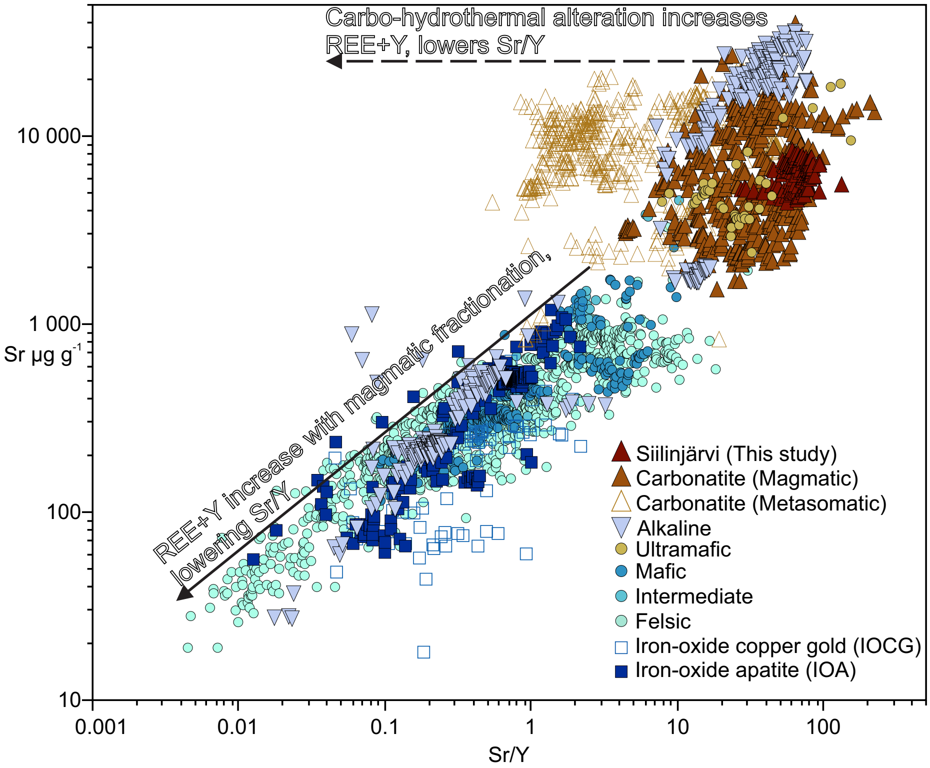

Fig. 8 Apatite Sr/Y versus Sr diagram. Sr/Y ratios are highest in apatite from carbonatites and ultramafic silicate rocks. Strontium concentrations and Sr/Y ratios decrease with increasing fractionation as REE+Y increases (solid line). In carbonatitic rocks, carbo-hydrothermal alteration drives the composition of apatite towards lower Sr/Y due to increasing REE+Y, especially HREE (stippled line). Siilinjärvi apatite is among the highest Sr/Y with average Sr concentrations. Notice the logarithmic scale on both axes. Data from Sha and Chappell 1999; O'Reilly and Griffin 2000; Belousova et al. 2001; Belousova et al. 2002; Brassinnes et al. 2005; Hsieh et al. 2008; Tollari et al. 2008; Chu et al. 2009; Xu et al. 2010; Bonyadi et al. 2011; Tang et al. 2012; Chen and Simonetti; 2013; Mao et al. 2016; Pan et al. 2016; Broom-Fendley et al. 2017; Chakhmouradian et al. 2017; Deng et al. 2017; Doroshkevich et al. 2017; Mukherjee et al. 2017; Jiang et al. 2018; Andersson et al. 2019; Du et al. 2019; Duan et al.; 2019; Hu et al. 2019; Palma et al. 2019; Qu et al. 2019; Ren et al. 2019; Wang et al. 2019; Yu et al. 2019; Zafar et al. 2019; Zhang et al. 2019; Jia et al. 2020; Mercer et al. 2020; Zhang et al. 2020; Broom-Fendley et al. 2021; Lu et al. 2021; Su et al. 2021; this study. The database is available online in Electronic Appendix B.

decreasing Sr/Y ratios and increasing REE+Y and enrichment in HREE (Broom-Fendley et al. 2017; Chakhmouradian et al. 2017; Lu et al. 2021).

High Sr/Y ratios similar to those from Siilinjärvi have been observed in some fluorapatite analyzed from the early-stage carbonatite of Songwe Hill (C1 calciocarbonatite, Malawi; Broom-Fendley et al. 2017), the Ulgii Khid carbonatite in Mongolia (Feng et al. 2020), carbonatites and ultramafic rocks from alkaline-ultramafic complexes in Russia (Vuoriyarvi, Turiy Peninsula, and Tiksheozero; Brassines et al. 2005; Mao et al. 2016; Kovdor, Broom-Fendley et al. 2021), carbonate fluorapatite from metasomatized mantle peridotites (O'Reilly and Griffin 2000), Manitou Islands, Canada (Mao et al. 2016), and Catalão, Brazil (Broom-Fendley et al. 2021) but are relatively scarce amongst the global array.

The highest Sr/Y ratios were observed in apatite from the Ulgii Khid carbonatite-alkaline complex in Mongolia (Feng et al. 2020). Apatite from this locality has high Sr (13 000 ± 1 600 µg g^{-1}) and low REE (2 400 ± 200 µg g^{-1}) contents. The Ulgii Khid calcite carbonatite evolved through fractional

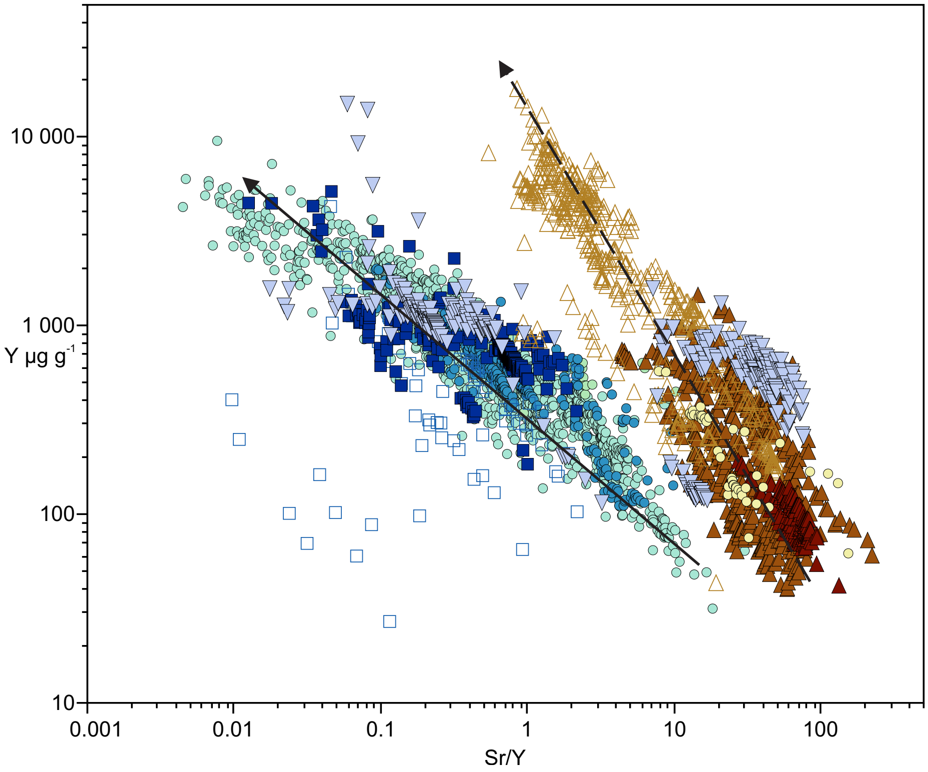

Fig. 9 Apatite Sr/Y versus Y diagram. Sr/Y ratios are highest in apatites from carbonatites and ultramafic silicate rocks. Strontium concentrations and Sr/Y ratios decrease with increasing fractionation as REE+Y increases. In carbonatitic rocks, carbo-hydrothermal alteration drives the composition of apatite towards lower Sr/Y due to increasing REE+Y. Notice the logarithmic scale on both axes. The symbols, colors, trend lines, and data sources are the same as in Fig. 8.

crystallization of a P-REE-rich carbonatite magma that formed through liquid immiscibility from a parental silicate magma (Feng et al. 2020). The Ulgii Khid apatites host melt inclusions with three immiscible phases (silicate, Fe-rich silicate, and phosphate melts). The low REE contents of Ulgii Khid apatites are due to the enrichment in Sr and REE likely preferentially partitioning into the phosphate melt and REE-rich phases (monazite, synchysite, parisite) in the calcite carbonatite. In the Songwe Hill carbonatite, the later carbonatite stages contain apatite with decreasing Sr/Y ratios and a progressive enrichment in HREE of up to 800 µg g^{-1} Yb in the late carbo-hydrothermal fluorite-apatite veins (Broom-Fendley et al. 2017). According to Broom-Fendley et al. (2017), such extreme HREE enrichment is caused by carbo-hydrothermal alteration from fluids derived from either the carbonatite itself (also supported by experimental petrology, Anenburg et al. 2020b), mixing of meteoric fluids with the fluids exsolved from the carbonatite or fluids derived from the nearby Mauze nepheline syenite intrusion.

The apatite with high Sr/Y ratios observed in this study and other magmatic carbonatites are hosted mostly by calcite carbonatites but also dolomite carbonatite and phoscorite (olivine-magnetite-apatite rock). This may indicate crystallization of apatite from similar magmas and fractionation paths. The high ratios likely represent early crystallizing apatite from relatively unfractionated carbonatite magma with no or little enrichment in REE and Y. This is due to the coupled substitution of REE and Y with Si or Na (Eq. 1, 2), causing REE to be largely incompatible in apatite in the absence of high Si or Na activities.

6. Summarizing statement and conclusions

This study presents discussion of a detailed major and trace element dataset from apatite of the Siilinjärvi complex in eastern Finland. The apatites generally have low REE, Na, and Si contents and high Sr/Y ratios. The Sr/Y ratios of the Siilinjärvi apatite are among the highest when compared to a global database of apatite compositions. We interpret the high Sr/Y ratios and strong depletion of HREE+Y to be inherited from the parental magma, which was likely derived from carbonated mantle, suggesting that the Siilinjärvi rocks represent cumulates fractionated from a carbonatite magma that have experienced variable post-magmatic modification. Some of the apatite crystals have REE-enriched rims that appear blue in CL images that have grown in contact with either a fractionated carbonatite magma, a brine-melt or a hydrothermal fluid that reacted with the apatite. In the Saarinen satellite pit, the apatite chemistry is further modified by deformation-related processes that led to recrystallization-reprecipitation in a fluid-rich regime and in the formation of monazite. Most of the apatite in Saarinen samples are low in Sr and F, enriched in Th, and contain abundant fluid inclusions.

The apatite in the Siilinjärvi complex is chemically heterogeneous but with a limited range of compositions. There are noticeable differences on all spatial scales, within a single crystal, between crystals in a sample, between samples and between the two sampling locations. The range of compositions in apatite is limited. The comparison of different generations of apatite and their proximity to dikes and veins or structural boundary zones allows for deciphering mineral reactions with the fluids. Utilizing modern analytical techniques to conduct a comprehensive study of fluid inclusions, and possible melt inclusions, of all the lithologies of the Siilinjärvi complex may elucidate the chemical composition and the origin of these melts and fluids and generate further insights into both emplacement temperatures and pressures of the complex.

Acknowledgements

We thank Michael Anenburg and Sam Broom-Fendley for their thoughtful feedback and comments on this manuscript. Michael Anenburg and an anonymous reviewer are also thanked for providing feedback on a previous version of this manuscript. S. Karvinen and A. Heinonen acknowledge financial support from the K.H. Renlund’s Foundation for a doctoral fellowship, and S. Karvinen acknowledges the Nordenskiöld Foundation for additional financial support for analytical costs. We thank Mikko Savolainen, formerly of Yara Suomi Oy, for providing the Siilinjärvi rock samples and Paula Bigler for helping with the study area map. We acknowledge the help and support of Juhani Virkanen and Adam Abersteiner during the LA-ICP-MS analyses. S. Karvinen and C. Beier acknowledge a stay at the Iloranta resort during which this manuscript was being refined. This is HelLabs publication number #0017.

Supplementary Data

Electronic Appendices are available via Bulletin of the Geological Society Finland web page.

Electronic Appendix A: Results of in situ apatite mineral chemistry analyses and descriptions of analytical methods.

Electronic Appendix B: Global apatite trace element database. Consists of the results of this study and published apatite trace element data from literature.

Electronic Appendix C: Additional rare earth element (REE) binary diagrams of the results.

References

Al-Ani, T., 2013. Mineralogy and Petrography of Siilinjärvi Carbonatite and Glimmerite Rocks. Geological Survey of Finland, Report 164. https://tupa.gtk.fi/raportti/arkisto/164_2013.pdf

Andersen, A.K., Clark, J.G., Larson, P.B. & Donovan, J.J., 2017. REE fractionation, mineral speciation, and supergene enrichment of the Bear Lodge carbonatites, Wyoming, USA. Ore Geology Reviews 89, 780–807. https://doi.org/10.1016/j.oregeorev.2017.06.025

Andersson, S.S., Wagner, T., Jonsson, E., Fusswinkel, T. & Whitehouse, M.J., 2019. Apatite as a tracer of the source, chemistry and evolution of ore-forming fluids: The case of the Olserum-Djupedal REE-phosphate mineralisation, SE Sweden. Geochimica et Cosmochimica Acta 255, 163–187. https://doi.org/10.1016/j.gca.2019.04.014

Anenburg, M., Broom-Fendley, S. & Chen, W., 2021. Formation of Rare Earth Deposits in Carbonatites. Elements 17, 327–332. https://doi.org/10.2138/gselements.17.5.327

Anenburg, M., Mavrogenes, J.A. & Bennett, V.C., 2020a. The Fluorapatite P–REE–Th Vein Deposit at Nolans Bore: Genesis by Carbonatite Metasomatism. Journal of Petrology 61, egaa003.
https://doi.org/10.1093/petrology/egaa003

Anenburg, M., Mavrogenes, J.A., Frigo, C. & Wall, F., 2020b. Rare earth element mobility in and around carbonatites controlled by sodium, potassium, and silica. Sci. Adv. 6. https://doi.org/10.1126/sciadv.abb6570

Antignano, A. & Manning, C.E., 2008. Fluorapatite solubility in H_2O and H_2O–NaCl at 700 to 900°C and 0.7 to 2.0 GPa. Chemical Geology 251, 112–119. https://doi.org/10.1016/j.chemgeo.2008.03.001

Bell, K., Kjarsgaard, B.A. & Simonetti, A., 1998. Carbonatites—Into the Twenty-First Century. Journal of Petrology 39, 1839–1845. https://doi.org/10.1093/petroj/39.11-12.1839

Belousova, E.A., Walters, S., Griffin, W.L. & O'Reilly, S.Y., 2001. Trace-element signatures of apatites in granitoids from the Mt Isa Inlier, northwestern Queensland. Australian Journal of Earth Sciences 48, 603–619. https://doi.org/10.1046/j.1440-0952.2001.00879.x

Belousova, E.A., Griffin, W.L., O'Reilly & S.Y., Fisher, N.I., 2002. Apatite as an indicator mineral for mineral exploration: trace-element compositions and their relationship to host rock type. Journal of Geochemical Exploration 76, 45–69. https://doi.org/10.1016/S0375-6742(02)00204-2

Binder, G. & Troll, G., 1989. Coupled anion substitution in natural carbon-bearing apatites. Contributions to Mineralogy and Petrology 101, 394–401. https://doi.org/10.1007/BF00372213

Bonyadi, Z., Davidson, G.J., Mehrabi, B., Meffre, S. & Ghazban, F., 2011. Significance of apatite REE depletion and monazite inclusions in the brecciated Se–Chahun iron oxide–apatite deposit, Bafq district, Iran: Insights from paragenesis and geochemistry. Chemical Geology 281, 253–269. https://doi.org/10.1016/j.chemgeo.2010.12.013

Boudreau, A.E. & McCallum, I.S., 1989. Investigations of the Stillwater Complex: Part V. Apatites as indicators of evolving fluid composition. Contributions to Mineralogy and Petrology 102, 138–153. https://doi.org/10.1007/BF00375336

Brassinnes, S., Balaganskaya, E. & Demaiffe, D., 2005. Magmatic evolution of the differentiated ultramafic, alkaline and carbonatite intrusion of Vuoriyarvi (Kola Peninsula, Russia). A LA-ICP-MS study of apatite. Lithos 85, 76–92. https://doi.org/10.1016/j.lithos.2005.03.017

Broom-Fendley, S., Brady, A.E., Wall, F., Gunn, G. & Dawes, W., 2017. REE minerals at the Songwe Hill carbonatite, Malawi: HREE-enrichment in late-stage apatite. Ore Geology Reviews 81, 23–41. https://doi.org/10.1016/j.oregeorev.2016.10.019

Broom-Fendley, S., Siegfried, P.R., Wall, F., O'Neill, M., Brooker, R.A., Fallon, E.K., Pickles, J.R. & Banks, D.A., 2021. The origin and composition of carbonatite-derived carbonate-bearing fluorapatite deposits. Mineralium Deposita 56, 863–884. https://doi.org/10.1007/s00126-020-01010-7

Broom-Fendley, S., Styles, M.T., Appleton, J.D., Gunn, G. & Wall, F., 2016. Evidence for dissolution-reprecipitation of apatite and preferential LREE mobility in carbonatite-derived late-stage hydrothermal processes. American Mineralogist 101, 596–611. https://doi.org/10.2138/am-2016-5502CCBY

Bruand, E., Fowler, M., Storey, C., Laurent, O., Antoine, C., Guitreau, M., Heilimo, E. & Nebel, O., 2020. Accessory mineral constraints on crustal evolution: elemental fingerprints for magma discrimination. Geochemical Perspectives Letters 7.
https://doi.org/10.7185/geochemlet.2006

Bühn, B., 2008. The role of the volatile phase for REE and Y fractionation in low-silica carbonate magmas: implications from natural carbonatites, Namibia. Mineralogy and Petrology 92, 453–470. https://doi.org/10.1007/s00710-007-0214-4

Castor, S.B., 2008. The Mountain Pass Rare-Earth Carbonatite and Associated Ultrapotassic Rocks, California. Canadian Mineralogist 46:779–806. https://doi.org/10.3749/canmin.46.4.779

Chakhmouradian, A.R., 2006. High-field-strength elements in carbonatitic rocks: Geochemistry, crystal chemistry and significance for constraining the sources of carbonatites. Chemical Geology 235, 138–160.
https://doi.org/10.1016/j.chemgeo.2006.06.008

Chakhmouradian, A.R., Reguir, E.P. & Zaitsev, A.N., 2016. Calcite and dolomite in intrusive carbonatites. I. Textural variations. Mineralogy and Petrology 110, 333–360. https://doi.org/10.1007/s00710-015-0390-6

Chakhmouradian, A.R., Reguir, E.P., Zaitsev, A.N., Couëslan, C., Xu, C., Kynický, J., Mumin, A.H. & Yang, P., 2017. Apatite in carbonatitic rocks: Compositional variation, zoning, element partitioning and petrogenetic significance. Lithos 274–275, 188–213. https://doi.org/10.1016/j.lithos.2016.12.037

Simonetti, A., 2013. In-situ determination of major and trace elements in calcite and apatite, and U–Pb ages of apatite from the Oka carbonatite complex: Insights into a complex crystallization history. Chemical Geology 353, 151–172. https://doi.org/10.1016/j.chemgeo.2012.04.022

Chu, M.-F., Wang, K.-L., Griffin, W.L., Chung, S.-L., O'Reilly, S.Y., Pearson, N.J. & Iizuka, Y., 2009. Apatite Composition: Tracing Petrogenetic Processes in Transhimalayan Granitoids. Journal of Petrology 50, 1829–1855. https://doi.org/10.1093/petrology/egp054

Decrée, S., Cawthorn, G., Deloule, E., Mercadier, J., Frimmel, H. & Baele, J.-M., 2020a. Unravelling the processes controlling apatite formation in the Phalaborwa Complex (South Africa) based on combined cathodoluminescence, LA-ICPMS and in-situ O and Sr isotope analyses. Contributions to Mineralogy and Petrology 175, 34. https://doi.org/10.1007/s00410-020-1671-6

Decrée, S., Savolainen, M., Mercadier, J., Debaille, V., Höhn, S., Frimmel, H. & Baele, J.-M., 2020b. Geochemical and spectroscopic investigation of apatite in the Siilinjärvi carbonatite complex: Keys to understanding apatite forming processes and assessing potential for rare earth elements. Applied Geochemistry 123, 104778. https://doi.org/10.1016/j.apgeochem.2020.104778

Deng, M., Xu, C., Song, W., Tang, H., Liu, Y., Zhang, Q., Zhou, Y., Feng, M. & Wei, C., 2017. REE mineralization in the Bayan Obo deposit, China: Evidence from mineral paragenesis. Ore Geology Reviews 91, 100–109. https://doi.org/10.1016/j.oregeorev.2017.10.018

Dill, H.G. 1994. Can REE patterns and U-Th variations be used as a tool to determine the origin of apatite in clastic rocks? Sedimentary Geology 92, 175–196. https://doi.org/10.1016/0037-0738(94)90105-8

Doroshkevich, A.G., Veksler, I.V., Klemd, R., Khromova, E.A. & Izbrodin, I.A., 2017. Trace-element composition of minerals and rocks in the Belaya Zima carbonatite complex (Russia): Implications for the mechanisms of magma evolution and carbonatite formation. Lithos 284–285, 91–108. https://doi.org/10.1016/j.lithos.2017.04.003

Du, J., Wang, G. & Jia, L., 2019. In situ major and trace element compositions of apatites from Luanchuan orecluster: Implications for porphyry Mo mineralization. Ore Geology Reviews 115, 103174. https://doi.org/10.1016/j.oregeorev.2019.103174

Duan, X., Chen, B., Sun, K., Wang, Z., Yan, X. & Zhang, Z., 2019. Accessory mineral chemistry as a monitor of petrogenetic and metallogenetic processes: A comparative study of zircon and apatite from Wushan Cu- and Zhuxiling W(Mo)-mineralization-related granitoids. Ore Geology Reviews 111, 102940. https://doi.org/10.1016/j.oregeorev.2019.102940

Elliott, H.A.L., Wall, F., Chakhmouradian, A.R., Siegfried, P.R., Weatherley, S., Finch, A.A., Marks, M.A.W., Dowman, E. & Deady, E. 2018. Fenites associated with carbonatite complexes: A review. Ore Geology Reviews 22. https://doi.org/10.1016/j.oregeorev.2017.12.003

Fan, H.-R., Yang, K.-F., Hu, F.-F., Liu, S. & Wang, K.-Y., 2016. The giant Bayan Obo REE-Nb-Fe deposit, China: Controversy and ore genesis. Geoscience Frontiers 7, 335–344. https://doi.org/10.1016/j.gsf.2015.11.005

Feng, M., Song, W., Kynicky, J., Smith, M., Cox, C., Kotlanova, M., Brtnicky, G.H., Wei, F. & Wei, C. 2020. Primary rare earth element enrichment in carbonatites: Evidence from melt inclusions in Ulgii Khiid carbonatite, Mongolia. Ore Geology Reviews 117, 103294. https://doi.org/10.1016/j.oregeorev.2019.103294

Fleet, M.E. & Pan, Y., 1995. Site preference of rare earth elements in fluorapatite. American Mineralogist 80, 329–335. https://doi.org/10.2138/am-1995-3-414

Goldoff, B., Webster, J.D. & Harlov, D.E., 2012. Characterization of fluor-chlorapatites by electron probe microanalysis with a focus on time-dependent intensity variation of halogens. American Mineralogist 97, 1103–1115. https://doi.org/10.2138/am.2012.3812

Götze, J., 2012. Application of Cathodoluminescence Microscopy and Spectroscopy in Geosciences. Microscopy and Microanalysis 18, 1270–1284. https://doi.org/10.1017/S1431927612001122

Guillong, M., 2008. SILLS: A MATLAB-based program for the reduction of laser ablation ICP-MS data of homogeneous materials and inclusions. In: Sylvester, P. (Ed.), Laser Ablation ICP-MS in the Earth Sciences: Current Practices and Outstanding Issues: Mineralogical Association of Canada Short Course Series, vol. 40, pp. 328–333.

Guzmics T., Mitchell R.H., Szabó C., Berkesi M., Milke R. & Abart R. 2011. Carbonatite melt inclusions in coexisting magnetite, apatite and monticellite in Kerimasi calciocarbonatite, Tanzania: melt evolution and petrogenesis. Contributions to Mineralogy and Petrology 161, 177–96 https://doi.org/10.1007/s00410-010-0525-z

Harlov, D.E., 2015. Apatite: A Fingerprint for Metasomatic Processes. Elements 11, 171–176. https://doi.org/10.2113/gselements.11.3.171

Harlov, D.E. & Förster, H.-J., 2003. Fluid-induced nucleation of (Y+REE)-phosphate minerals within apatite: Nature and experiment. Part II. Fluorapatite. American Mineralogist 88, 1209–1229. https://doi.org/10.2138/am-2003-8-905

Harlov, D.E., Förster, H.-J. & Nijland, T.G., 2002. Fluid-induced nucleation of (Y + REE)-phosphate minerals within apatite: Nature and experiment. Part I. Chlorapatite. American Mineralogist 87, 245–261. https://doi.org/10.2138/am-2002-2-306

Harlov, D.E., Wirth, R. & Förster, H.-J., 2005. An experimental study of dissolution–reprecipitation in fluorapatite: fluid infiltration and the formation of monazite. Contributions to Mineralogy and Petrology 150, 268–286. https://doi.org/10.1007/s00410-005-0017-8

Hölttä, P., Balagansky, V., Garde, A.A., Mertanen S., Peltonen P., Slabunov A., Ward P.S. & Whitehouse M, 2008. Archean of Greenland and Fennoscandia. Episodes

31, 13–19. https://doi.org/10.18814/epiiugs/2008/v31i1/003

Hornig-Kjarsgaard, I., 1998. Rare Earth Elements in Sövitic Carbonatites and their Mineral Phases. Journal of Petrology 39, 2105–2121. https://doi.org/10.1093/petroj/39.11-12.2105

Hou, Z., Liu, Y., Tian, S., Yang, Z. & Xie, Y., 2015. Formation of carbonatite-related giant rare-earth-element deposits by the recycling of marine sediments. Scientific Reports 5, 10231. https://doi.org/10.1038/srep10231

Hsieh, P.-S., Chen, C.-H., Yang, H.-J. & Lee, C.-Y., 2008. Petrogenesis of the Nanling Mountains granites from South China: Constraints from systematic apatite geochemistry and whole-rock geochemical and Sr–Nd isotope compositions. Journal of Asian Earth Sciences 33, 428–451. https://doi.org/10.1016/j.jseaes.2008.02.002

Hu, L., Li, Y.-K., Wu, Z., Bai, Y. & Wang, A., 2019. Two metasomatic events recorded in apatite from the ore-hosting dolomite marble and implications for genesis of the giant Bayan Obo REE deposit, Inner Mongolia, Northern China. Journal of Asian Earth Sciences 172, 56–65. https://doi.org/10.1016/j.jseaes.2018.08.022

Hughes, J.M., Cameron, M. & Crowley, K.D., 1991. Ordering of divalent cations in the apatite structure: Crystal structure refinements of natural Mn- and Sr-bearing apatite. American Mineralogist 76, 1857–1862.

Humphreys-Williams, E.R. & Zahirovic, S., 2021. Carbonatites and Global Tectonics. Elements 17, 339–344. https://doi.org/10.2138/gselements.17.5.339

Janoušek, V., Farrow, C. M. & Erban, V. 2006. Interpretation of whole-rock geochemical data in igneous geochemistry: introducing Geochemical Data Toolkit (GCDkit). Journal of Petrology 476, 1255–1259. https://doi.org/10.1093/petrology/egl013

Jarosewich, E., Nelen, J.A. & Norberg, J.A., 1980. Reference samples for electron microprobe analysis. Geostandard Newsletter 4, 43-47. https://doi.org/10.1111/j.1751-908X.1980.tb00273.x

Jia, F., Zhang, C., Liu, H., Meng, X. & Kong, Z., 2020. In situ major and trace element compositions of apatite from the Yangla skarn Cu deposit, southwest China: Implications for petrogenesis and mineralization. Ore Geology Reviews 127, 103360. https://doi.org/10.1016/j.oregeorev.2020.103360

Jiang, X.-Y., Li, H., Ding, X., Wu, K., Guo, J., Liu, J.-Q. & Sun, W.-D., 2018. Formation of A-type granites in the Lower Yangtze River Belt: A perspective from apatite geochemistry. Lithos 304–307, 125–134. https://doi.org/10.1016/j.lithos.2018.02.005

Kempe, U. & Götze, J., 2002. Cathodoluminescence (CL) behaviour and crystal chemistry of apatite from rare-metal deposits. Mineralogical Magazine 66, 151–172. https://doi.org/10.1180/0026461026610019

Ketcham, R.A., 2015. Technical Note: Calculation of stoichiometry from EMP data for apatite and other phases with mixing on monovalent anion sites. American Mineralogist 100, 1620–1623. https://doi.org/10.2138/am-2015-5171

Klemme, S. & Dalpé, C., 2003. Trace-element partitioning between apatite and carbonatite melt. American Mineralogist, 88, 639–646.

Lahtinen, R., Johnston, S.T., & Nironen, M., 2014. The Bothnian coupled oroclines of the Svecofennian Orogen: a Palaeoproterozoic terrane wreck. Terra Nova 26, 330–335. https://doi.org/10.1111/ter.12107

Le Bas, M.J., 1981. Carbonatite magmas. Mineralogical Magazine 44, 133–140. https://doi.org/10.1180/minmag.1981.044.334.02

Le Bas, M.J. & Handley, C.D., 1979. Variation in apatite composition in ijolitic and carbonatitic igneous rocks. Nature 279, 54–56. https://doi.org/10.1038/279054a0

Lee, M. J., Garcia, D., Moutte, J. & Lee, J. I, 2003. Phlogopite and tetraferriphlogopite from phoscorite and carbonatite associations in the Sokli massif, Northern Finland. Geosciences Journal 7, 9–20. https://doi.org/10.1007/BF02910260

Li, X.-C., Harlov, D.E., Zhou, M.-F. & Hu, H., 2022. Metasomatic modification of Sr isotopes in apatite as a function of fluid chemistry. Geochimica et Cosmochimica Acta 323, 123–140. https://doi.org/10.1016/j.gca.2022.02.025

Lu, J., Chen, W., Ying, Y., Jiang, S. & Zhao, K., 2021. Apatite texture and trace element chemistry of carbonatite-related REE deposits in China: Implications for petrogenesis. Lithos 398–399, 106276. https://doi.org/10.1016/j.lithos.2021.106276

Ma, R. L., Chen, W. T., Zhang, W. & Chen, Y. W. 2021. Hydrothermal upgrading as an important tool for the REE mineralization in the Miaoya carbonatite-syenite complex, Central China. American Mineralogist 106, 1690–1703. https://doi.org/10.2138/am-2021-7779

Mao, M., Rukhlov, A.S., Rowins, S.M., Spence, J. & Coogan, L.A., 2016. Apatite Trace Element Compositions: A Robust New Tool for Mineral Exploration. Economic Geology 111, 1187–1222. https://doi.org/10.2113/econgeo.111.5.1187

Mattsson, H.B., Högdahl, K., Carlsson, M. & Malehmir, A., 2019. The role of mafic dykes in the petrogenesis of the Archean Siilinjärvi carbonatite complex, east-central Finland. Lithos 342–343, 468–479. https://doi.org/10.1016/j.lithos.2019.06.011

Mercer, C. N., Watts, K. E. & Gross, J. 2020. Apatite trace element geochemistry and cathodoluminescent textures—A comparison between regional magmatism and the Pea Ridge IOAREE and Boss IOCG deposits, southeastern Missouri iron metallogenic province, USA. Ore Geology Reviews 116, 103129. https://doi.org/10.1016/j.oregeorev.2019.103129

Merlet, C., 1994. An accurate computer correction program for quantitative electron probe microanalysis. Microchimica

Acta 114-115, 363–376. https://doi.org/10.1007/BF01244563

McCubbin, F.M., Steele, A., Nekvasil, H., Schnieders, A., Rose, T., Fries, M., Carpenter, P.K. & Jolliff, B.L., 2010. Detection of structurally bound hydroxyl in fluorapatite from Apollo Mare basalt 15058,128 using TOF-SIMS. American Mineralogist 95, 1141–1150. https://doi.org/10.2138/am.2010.3448

McDonough, W.F. & Sun, S. -s., 1995. The composition of the Earth. Chemical Geology 120, 223–253. https://doi.org/10.1016/0009-2541(94)00140-4

Mitchell, R.H., 2005. Carbonatites and carbonatites and carbonatites. Canadian Mineralogist 43:2049–2068. https://doi.org/10.2113/gscanmin.43.6.2049

Mukherjee, R., Venkatesh, A.S. & Fareeduddin, 2017. Chemistry of magnetite-apatite from albitite and carbonate-hosted Bhukia Gold Deposit, Rajasthan, western India – An IOCG-IOA analogue from Paleoproterozoic Aravalli Supergroup: Evidence from petrographic, LA-ICP-MS and EPMA studies. Ore Geology Reviews 91, 509–529. https://doi.org/10.1016/j.oregeorev.2017.09.005

Nabyl, Z., 2020. A window in the course of alkaline magma differentiation conducive to immiscible REE-rich carbonatites. Geochimica et Cosmochimica Acta 27, 297–323. https://doi.org/10.1016/j.gca.2020.04.008

Nielsen, C. H. & Sigurdsson, H. 1981. Quantitative methods for electron microprobe analysis of sodium in natural and synthetic glasses. American Mineralogist 66, 547–552.

Nironen, M., 2017. Guide to the geological map of Finland – Bedrock 1:1 000 000. – Major stratigraphic units, metamorphism and tectonic evolution. Geological Survey of Finland, Special Paper 60, 41–76

O'Brien, H., Heilimo, E. & Heino, P., 2015. Chapter 4.3 - The Archean Siilinjärvi Carbonatite Complex, in: Maier, W.D., Lahtinen, R., O'Brien, Hugh (Eds.), Mineral Deposits of Finland. Elsevier, pp. 327–343. https://doi.org/10.1016/B978-0-12-410438-9.00013-3

O'Reilly, S.Y. & Griffin, W.L., 2000. Apatite in the mantle: implications for metasomatic processes and high heat production in Phanerozoic mantle. Lithos 53, 217–232. https://doi.org/10.1016/S0024-4937(00)00026-8

O'Sullivan, G., Chew, D., Kenny, G., Henrichs, I. & Mulligan, D. 2020. The trace element composition of apatite and its application to detrital provenance studies. Earth-Science Reviews 201 https://doi.org/10.1016/j.earscirev.2019.103044

Palma, G., Barra, F., Reich, M., Valencia, V., Simon, A.C., Vervoort, J., Leisen, M. & Romero, R., 2019. Halogens, trace element concentrations, and Sr-Nd isotopes in apatite from iron oxide-apatite (IOA) deposits in the Chilean iron belt: Evidence for magmatic and hydrothermal stages of mineralization. Geochimica et Cosmochimica Acta 246, 515–540. https://doi.org/10.1016/j.gca.2018.12.019

Pan, L.-C., Hu, R.-Z., Wang, X.-S., Bi, X.-W., Zhu, J.-J. & Li, C., 2016. Apatite trace element and halogen compositions as petrogenetic-metallogenic indicators: Examples from four granite plutons in the Sanjiang region, SW China. Lithos 254–255, 118–130. https://doi.org/10.1016/j.lithos.2016.03.010

Pasero, M., Kampf, A.R., Ferraris, C., Pekov, I.V., Rakovan, J. & White, T.J., 2010. Nomenclature of the apatite supergroup minerals. European Journal of Mineralogy 22, 163–179.
https://doi.org/10.1127/0935-1221/2010/0022-2022

Patiño Douce, A.E., Roden, M.F., Chaumba, J., Fleisher, C. & Yogodzinski, G., 2011. Compositional variability of terrestrial mantle apatites, thermodynamic modeling of apatite volatile contents, and the halogen and water budgets of planetary mantles. Chemical Geology 288, 14–31. https://doi.org/10.1016/j.chemgeo.2011.05.018

Pedersen, J. M., Ulrich, T., Whitehouse, M. J., Kent, A. J. & Tegner, C. 2021. The volatile and trace element composition of apatite in the Skaergaard intrusion, East Greenland. Contributions to Mineralogy and Petrology 176. https://doi.org/10.1007/s00410-021-01861-x

Piccoli, P. & Candela, P., 1994. Apatite in felsic rocks; a model for the estimation of initial halogen concentrations in the Bishop Tuff (Long Valley) and Tuolumne Intrusive Suite (Sierra Nevada Batholith) magmas. American Journal of Science 294, 92. https://doi.org/10.2475/ajs.294.1.92

Pouchou, J.-L. & Pichoir, F., 1991. Quantitative Analysis of Homogeneous or Stratified Microvolumes Applying the Model "PAP," in: Heinrich, K.F.J., Newbury, D.E. (Eds.), Electron Probe Quantitation. Springer US, Boston, MA, pp. 31–75. https://doi.org/10.1007/978-1-4899-2617-3_4

Poletti, J. E., Cottle, J. M., Hagen-Peter, G. A. & Lackey, J. S., 2016. Petrochronological constraints on the origin of the Mountain Pass ultrapotassic and carbonatite intrusive suite, California. Journal of Petrology 57, 1555–1598. https://doi.org/10.1093/petrology/egw050

Poutiainen, M. 1995. Fluids in the Siilinjärvi carbonatite complex, eastern Finland: Fluid inclusion evidence for the formation conditions of zircon and apatite. Bulletin of the Geolocial Society of Finland 67, 3–18. https://doi.org/10.17741/bgsf/67.1.001

Putnis, A., 2009. Mineral Replacement Reactions. Reviews in Mineralogy and Geochemistry 70, 87–124. https://doi.org/10.2138/rmg.2009.70.3

Puustinen, K. 1971. Geology of the Siilinjärvi carbonatite complex, Eastern Finland. Bulletin de la Commission Géologique de Finlande 249, 1–43. https://tupa.gtk.fi/julkaisu/bulletin/bt_249.pdf

Puustinen, K. 1972. Richterite and actinolite from the Siilinjärvi carbonatite complex, Finland. Bulletin of the Geolocial Society of Finland 44, 83–86. https://doi.org/10.17741/bgsf/44.1.007

Puustinen, K. 1973. Tetraferriphlogopite from the Siilinjärvi carbonatite complex. Finland. Bulletin of the Geolocial Society of Finland 45, 35–42. https://doi.org/10.17741/bgsf/45.1.005

Puustinen, K. 1974. Dolomite exsolution textures in calcite from the Siilinjärvi carbonatite complex, Finland. Bulletin of the Geolocial Society of Finland 46, 151–159. https://doi.org/10.17741/bgsf/46.2.008

Ranta, E., Stockmann, G., Wagner, T., Fusswinkel, T., Sturkell, E., Tollefsen, E. & Skelton, A. 2018. Fluid–rock reactions in the 1.3 Ga siderite carbonatite of the Grønnedal–Íka alkaline complex, Southwest Greenland. Contributions to Mineralogy and Petrology 173, 1–26. https://doi.org/10.1007/s00410-018-1505-y

Rønsbo, J.G., 1989. Coupled substitutions involving REEs and Na and Si in apatites in alkaline rocks from the Ilimaussaq Intrusion, South Greenland, and the petrological implications. American Mineralogist 74, 896–901.

Qu, P., Li, N.-B., Niu, H.-C., Yang, W.-B., Shan, Q. & Zhang, Z.-Y., 2019. Zircon and apatite as tools to monitor the evolution of fractionated I-type granites from the central Great Xing'an Range, NE China. Lithos 348–349, 105207. https://doi.org/10.1016/j.lithos.2019.105207

Ren, Y., Yang, X., Wang, S. & Öztürk, H., 2019. Mineralogical and geochemical study of apatite and dolomite from the Bayan Obo giant Fe-REE-Nb deposit in Inner Mongolia: New evidences for genesis. Ore Geology Reviews 109, 381–406. https://doi.org/10.1016/j.oregeorev.2019.04.020

Roeder, P.L., MacArthur, D., Ma, X.-P., Palmer, G.R. & Mariano, A.N., 1987. Cathodoluminescence and microprobe study of rare-earth elements in apatite. American Mineralogist 72, 801–811.

Rønsbo, J.G., 1989. Coupled substitutions involving REEs and Na and Si in apatites in alkaline rocks from the Ilimaussaq Intrusion, South Greenland, and the petrological implications. American Mineralogist 74, 896–901.

Rukhlov, A.S. & Bell, K., 2010. Geochronology of carbonatites from the Canadian and Baltic Shields, and the Canadian Cordillera: clues to mantle evolution. Mineralogy and Petrology 98, 11–54. https://doi.org/10.1007/s00710-009-0054-5

Sartori, G., Galli, A., Weidendorfer, D. & Schmidt, M.W. 2022. A tool to distinguish magmatic from secondarily recrystallized carbonatites—Calcite/apatite rare earth element partitioning. *Geology* 51, 54–58. https://doi.org/10.1130/G50416.1

Sartori, G. & Schmidt, M. W. 2023. Phosphorous-solubility in carbonatite melts: Apatite crystallization modeled via its solubility product. Geochimica et Cosmochimica Acta 352, 122–132. https://doi.org/10.1016/j.gca.2023.04.034

Schmidt, M.W. & Weidendorfer, D., 2018. Carbonatites in oceanic hotspots. Geology 46, 435–438. https://doi.org/10.1130/G39621.1

Sha, L.-K. & Chappell, B.W., 1999. Apatite chemical composition, determined by electron microprobe and laser-ablation inductively coupled plasma mass spectrometry, as a probe into granite petrogenesis. Geochimica et Cosmochimica Acta 63, 3861–3881. https://doi.org/10.1016/S0016-7037(99)00210-0

Slezak, P., Spandler, C. & Blake, K. 2018. Ghosts of apatite past: using hyperspectral cathodoluminescence and micro-geochemical data to reveal multi-generational apatite in the Gifford Creek Carbonatite Complex, Australia. Canadian Mineralogist 56, 773–797. https://doi.org/10.3749/canmin.1800021

Sorjonen-Ward, P. & Luukkonen, E. J. 2005. Archean rocks. Developments in Precambrian geology 14, 19–99. Elsevier. https://doi.org/10.1016/S0166-2635(05)80003-9.

Spandler, C., Pettke, T. & Rubatto, D., 2011. Internal and External Fluid Sources for Eclogite-facies Veins in the Monviso Meta-ophiolite, Western Alps: Implications for Fluid Flow in Subduction Zones. Journal of Petrology 52, 1207–1236. https://doi.org/10.1093/petrology/egr025

Stock, M.J., Humphreys, M.C.S., Smith, V.C., Johnson, R.D., Pyle, D.M. & EIMF, 2015. New constraints on electron-beam induced halogen migration in apatite. American Mineralogist 100, 281–293. https://doi.org/10.2138/am-2015-4949

Stormer, J.C., Pierson, M.L. & Tacker, R.C., 1993. Variation of F and Cl X-ray intensity due to anisotropic diffusion in apatite during electron microprobe analysis. American Mineralogist 78, 641–648.

Su, JH., Zhao, XF., Li, XC., Su, ZK., Liu, R., Qin, ZJ. & Chen, M., 2021. Fingerprinting REE mineralization and hydrothermal remobilization history of the carbonatite-alkaline complexes, Central China: Constraints from in situ elemental and isotopic analyses of phosphate minerals. American Mineralogist 106, 1545–1558. https://doi.org/10.2138/am-2021-7746

Tacker, R.C., 2008. Carbonate in igneous and metamorphic fluorapatite: Two type A and two type B substitutions. American Mineralogist 93, 168–176. https://doi.org/10.2138/am.2008.2551

Tang, M., Wang, X.-L., Xu, X.-S., Zhu, C., Cheng, T. & Yu, Y., 2012. Neoproterozoic subducted materials in the generation of Mesozoic Luzong volcanic rocks: Evidence from apatite geochemistry and Hf–Nd isotopic decoupling. Gondwana Research 21, 266–280. https://doi.org/10.1016/j.gr.2011.05.009

Tichomirowa, M., Grosche, G., Gotze, J., Belyatsky, B., Savva, E., Keller, J. & Todt, W., 2006. The mineral isotope composition of two Precambrian carbonatite complexes from the Kola Alkaline Province – Alteration versus primary magmatic signatures. Lithos 91, 229–249. https://doi.org/10.1016/j.lithos.2006.03.019

Tichomirowa, M., Whitehouse, M.J., Gerdes, A., Götze, J., Schulz, B. & Belyatsky, B.V., 2013. Different zircon recrystallization types in carbonatites caused by magma mixing: Evidence from U–Pb dating, trace element and isotope composition (Hf and O) of zircons from two Precambrian carbonatites from Fennoscandia. Chemical Geology 353, 173–198. https://doi.org/10.1016/j.chemgeo.2012.11.004

Tollari, N., Barnes, S.-J., Cox, R.A. & Nabil, H., 2008. Trace element concentrations in apatites from the Sept-Îles Intrusive Suite, Canada — Implications for the genesis of nelsonites. Chemical Geology 252, 180–190. https://doi.org/10.1016/j.chemgeo.2008.02.016

Walter, B.F., Giebel, R.J., Steele-MacInnis, M., Marks, M.A.W., Kolb, J. & Markl, G., 2021. Fluids associated with carbonatitic magmatism: A critical review and implications for carbonatite magma ascent. Earth-Science Reviews 215, 103509. https://doi.org/10.1016/j.earscirev.2021.103509

Wang, C., Liu, J., Zhang, H., Zhang, X., Zhang, D., Xi, Z. & Wang, Z., 2019. Geochronology and mineralogy of the Weishan carbonatite in Shandong province, eastern China. Geoscience Frontiers 10, 769–785. https://doi.org/10.1016/j.gsf.2018.07.008

Wang, Z.-Y., Fan, H.-R., Zhou, L., Yang, K.-F. & She, H.-D., 2020. Carbonatite-Related REE Deposits: An Overview. Minerals 10, 965. https://doi.org/10.3390/min10110965

Watson, E.B. & Green, T.H., 1981. Apatite/liquid partition coefficients for the rare earth elements and strontium. Earth and Planetary Science Letters 56, 405–421. https://doi.org/10.1016/0012-821X(81)90144-8

Webster, J. D. & Piccoli, P. M. 2015. Magmatic apatite: A powerful, yet deceptive, mineral. Elements 11, 177–182. https://doi.org/10.2113/gselements.11.3.177

Wei, C., Xu, C., Deng, M., Song, W., Shi, A., Li, Z., Fan, C. & Kuang, G., 2022. Origin of metasomatic fluids in the Bayan Obo rare-earth-element deposit. Ore Geology Reviews 141, 104654. https://doi.org/10.1016/j.oregeorev.2021.104654

Weidendorfer, D., Schmidt, M.W. & Mattsson, H.B., 2017. A common origin of carbonatite magmas. Geology 45, 507–510. https://doi.org/10.1130/G38801.1

Woolley, A.R. & Kjarsgaard, B.A., 2008. Paragenetic types of carbonatite as indicated by the diversity and relative abundances of associated silicate rocks: Evidence from a global database. Canadian Mineralogist 46:741–752. https://doi.org/10.3749/canmin.46.4.741

Xu, C., Kynicky, J., Chakhmouradian, A.R., Campbell, I.H. & Allen, C.M., 2010. Trace-element modeling of the magmatic evolution of rare-earth-rich carbonatite from the Miaoya deposit, Central China. Lithos 118, 145–155. https://doi.org/10.1016/j.lithos.2010.04.003

Yaxley, G. M., Anenburg, M., Tappe, S., Decrée, S. & Guzmics, T., 2022. Carbonatites: classification, sources, evolution, and emplacement. Annual Review of Earth and Planetary Sciences 50, 261–293. https://doi.org/10.1146/annurev-earth-032320-104243

Yi, H., Balan, E., Gervais, C., Segalen, L., Fayon, F., Roche, D., Person, A., Morin, G., Guillaumet, M., Blanchard, M., Lazzeri, M. & Babonneau, F., 2013. A carbonate-fluoride defect model for carbonate-rich fluorapatite. American Mineralogist 98, 1066–1069. https://doi.org/10.2138/am.2013.4445

Ying, Y.-C., Chen, W., Simonetti, A., Jiang, S.-Y. & Zhao, K.-D., 2020. Significance of hydrothermal reworking for REE mineralization associated with carbonatite: Constraints from in situ trace element and C-Sr isotope study of calcite and apatite from the Miaoya carbonatite complex (China). Geochimica et Cosmochimica Acta 280, 340–359. https://doi.org/10.1016/j.gca.2020.04.028

Yu, Z.-Q., Chen, W.-F., Chen, P.-R., Wang, K.-X., Fang, Q.-C., Tang, X.-S. & Ling, H.-F., 2019. Chemical composition and Sr isotopes of apatite in the Xiangshan A-type volcanic-intrusive complex, Southeast China: New insight into petrogenesis. Journal of Asian Earth Sciences 172, 66–82. https://doi.org/10.1016/j.jseaes.2018.08.019

Zafar, T., Leng, C.-B., Zhang, X.-C. & Rehman, H.U., 2019. Geochemical attributes of magmatic apatite in the Kukaazi granite from western Kunlun orogenic belt, NW China: Implications for granite petrogenesis and Pb-Zn (-Cu-W) mineralization. Journal of Geochemical Exploration 204, 256–269. https://doi.org/10.1016/j.gexplo.2019.06.005

Zhang, D., Liu, Y., Pan, J., Dai, T. & Bayless, R.C., 2019. Mineralogical and geochemical characteristics of the Miaoya REE prospect, Qinling orogenic Belt, China: Insights from Sr-Nd-C-O isotopes and LA-ICP-MS mineral chemistry. Ore Geology Reviews 110, 102932. https://doi.org/10.1016/j.oregeorev.2019.05.018

Zhang, X., Guo, F., Zhang, B., Zhao, L., Wu, Y., Wang, G. & Alemayehu, M., 2020. Magmatic evolution and post-crystallization hydrothermal activity in the early Cretaceous Pingtan intrusive complex, SE China: records from apatite geochemistry. Contributions to Mineralogy and Petrology 175, 35. https://doi.org/10.1007/s00410-020-1675-2

Zhou, B. Q., Yang, J. H., Sun, J. F., Wang, H., Zhu, Y. S., Wu, Y. D. & Xu, L. 2023. Apatite geochemical and Sr-Nd isotopic constraints on the source and petrogenesis of alkaline volcanic-plutonic ring complex. Lithos, 107334. https://doi.org/10.1016/j.lithos.2023.107334

Zirner, A.L.K., Marks, M.A.W., Wenzel, T., Jacob, D.E. & Markl, G., 2015. Rare earth elements in apatite as a monitor of magmatic and metasomatic processes: The Ilímaussaq complex, South Greenland. Lithos 228–229, 12–22. https://doi.org/10.1016/j.lithos.2015.04.013

Zozulya, D.R., Bayanova, T.B. & Serov, P.N., 2007. Age and isotopic geochemical characteristics of Archean carbonatites and alkaline rocks of the Baltic shield. Doklady Earth Sciences 415, 874–879. https://doi.org/10.1134/S1028334X07060104